Numerical Study of Grating Coupler for Beam Steering

by

Wei Guo

A thesis submitted in partial fulfillment
of the requirements for the degree of
Master of Science in Engineering
(Automotive Systems Engineering)
in the University of Michigan-Dearborn
2018

Master's Thesis Committee:

Professor Yasha Yi, Chair
Professor Weidong Xiang
Associate Professor Nilay Chakraborty

ACKNOWLEDGEMENTS

I would first like to thank my thesis advisor, Professor Yasha Yi, for the continuous support of my Master study and related research, for his kindness, patience and immense knowledge. His guidance helped me in the time of study and writing this thesis. Without his help, it would not be possible to conduct this research.

Also, I want to show my appreciation to my colleague Dachuan Wu, Mao Ye and Yueheng Peng for their help and company during the days at University of Michigan. I would like to thank all my friends for accepting nothing less than excellence from me.

Last but not the least, I must express my very profound gratitude to my parents for providing me with unfailing support and continuous encouragement throughout my years of study and through the process of researching and writing this thesis. This accomplishment would not have been possible without them. Thank you.

TABLE OF CONTENTS

ACKNOWLEDGEMENTS ii

LIST OF FIGURES v

ABSTRACT vii

Chapter I Research Background and Basic Theory of FDTD Simulation

1.1 Research Background 1

1.2 FDTD Simulation Method 3

1.3 Far-field Calculation 5

Chapter II Diffraction Grating theory and Grating coupler

2.1 Basic Design of Grating Coupler 8

2.2 Coupling Theory 10

2.2.1 Geometrical Theory 10

2.2.2 Bragg Theory of Periodic Media 11

2.2.3 K-Space Theory 16

2.3 Tunable Parameters for Beam Steering Application 18

Chapter III One Beam Steering

3.1 3D Simulation Analysis 20

3.2 Wavelength Tuning and Color Map 22

3.3 Effect of Grating Period Size 23

3.4 Research on the Number of Total Periods 27

3.5 Optimization of Etching Depth 29

Chapter IV Two Beams Steering

4.1 Single Periodicity for Two Beams Steering 32

4.2 Series Connection of Two Emitting Areas 34

4.3 Compound Grating Coupler for Multiple Beams Steering 35

4.3.1 Introduction of Compound Grating Coupler 35

4.3.2 Coupling Mechanism 36

4.3.3 Simulation Result Analysis 39

4.4 Optimization and Fabrication Tolerance 44

4.5 Conclusion 46

Chapter V Measurement and Analysis of Metalens

5.1 Introduction 48

5.2 Measurement of Linear Distinguishing Metalens 49

Chapter VI Conclusion 51

REFERENCES 52

APPENDIX: PUBLICATIONS 56

LIST OF FIGURES

Fig. 1.1 Illustration of using 4 solid state Lidars for full 360 detection range..... 2

Fig. 1.2 Illustration of the electric field diffraction pattern 6

Fig. 2.1 Basic model of the grating coupler..... 8

Fig. 2.2 Screenshot of one beam steering grating coupler..... 9

Fig. 2.3 Screenshot of the field distribution..... 9

Fig. 2.4 Illustration of beam coupling mechanism 10

Fig. 2.5 Electric field perturbed by structures (a) Single dielectric structure; (b) periodic structures..... 12

Fig. 2.6 Illustration of light on the incident to grating structure..... 14

Fig. 2.7 Reflection and transmission modes in the grating structure..... 15

Fig. 2.8 Illustration of a K-space diagram 16

Fig. 3.1 Illustration of the grating coupler 3-D model..... 20

Fig. 3.2 Normalized out-coupling angles..... 21

Fig. 3.3 The electric field distribution near the grating area..... 21

Fig. 3.4 Wavelength tuning map for single beam steering..... 22

Fig. 3.5 Illustration of 2D grating coupler with a periodicity of 650 nm 23

Fig. 3.6 Far-field simulation results with different periodicities 25

Fig. 3.7 K-space diagram of multiple out-coupling diffracted modes..... 26

Fig. 3.8 Grating periodicity vs. Angle of the diffracted order with the highest intensity..... 26

Fig. 3.9 Periodicity tuning map at a fixed input wavelength of 1550 nm..... 27

Fig. 3.10 Effect of the number of total periods on beam quality 28

Fig. 3.11 Effect of etching depth on beam quality (Depth 40 nm) 29

Fig. 3.12 Effect of etching depth on beam quality (Depth 50 nm) 30

Fig. 3.13 Effect of etching depth on beam quality (Depth 60 nm) 30

Fig. 3.14 Effect of etching depth on beam quality (Depth 70 nm) 31

Fig. 4.1 Periodicity (435 nm – 1000nm) tuning map..... 32

Fig. 4.2 Two beams simultaneously coupled out at the periodicity of 857 nm 33

Fig. 4.3 Illustration of series connected design for two beams coupling..... 34

Fig. 4.4 Far-field result of the series connected design at the input of 1550 nm 35

Fig. 4.5 Illustration of single period grating coupler. Λ is the periodicity, d is the grating depth, and θ is the out-coupling angle. 36

Fig. 4.6 Illustration of the compound period grating coupler structure 38

Fig. 4.7 Far-field simulation result of the compound period grating coupler with applied wavelength of 1550 nm. (a) Field distribution; (b) Normalized intensity 40

Fig. 4.8 Performance of compound period grating coupler V.S. Applied wavelength. (a) Far-field contour map; (b) Energy flow. 41

Fig. 4.9 Illustration of the structure without the gaps cannot be fabricated..... 44

Fig. 4.10 Performance of compound period grating coupler considering the fabrication tolerance of high aspect ratio gaps. (a) Far field contour map; (b) Energy flow. 45

Fig. 5.1 SEM image of the lens (a) Overall View of the Metalens; (b) Zoomed in Center Area (5×5 μm). 48

Fig. 5.2 Illustration of the optical characterization system 49

Fig. 5.3 Measurement results for Linear Distinguishing Metalens (a) Ez Direction; (b) Hz Direction 50

ABSTRACT

Emerging integrated photonic that studies the generation, processing, and detection of light in chip-scale optical media is one of the most important topics in modern optics research. Grating couplers have raised tremendous research interest due to its outstanding performance in compact non-mechanical beam steering, especially its potential applications in Solid State Lidar.

In this work, the mechanism of one beam free-space coupling is introduced, the effects of different parameters in the grating coupler design, such as period size, number of total periods and etching depth are simulated and analyzed by FDTD method. And base on the numerical study of one beam grating coupler, we proposed a novel design of a compound period grating coupler formed by combining two grating structures with different periodicities. The new compound period grating coupler structure can couple the waveguide mode into two radiation modes with different angles. Therefore, the beam steering range is doubled due to the extra beam. We numerically demonstrate this idea, and a $26.20°$ steering range is observed within a wavelength tuning range of 1500 nm to 1600 nm. In addition, the investigation of fabrication tolerance shows that the new structure can be fabricated with the current CMOS technology.

Chapter I

Research Background and Basic Theory of FDTD simulation

1.1 Research Background

The autonomous driving car has been developed for decades and in recent years the trend of being practical reaches to a top level because of the request of customers. Normally, an autonomous car is an integration of artificial intelligence and sensors, Light Detection and Ranging (LiDAR) belongs to one kind of the sensors and is found having several advantages compared to radar and camera.

Most companies developing self-driving vehicles seem to agree that the massive amount of long range, high accuracy data that you get from LIDAR is necessary, especially for complicated and variable urban environments. In other words, LIDAR is the most important sensor that is crucial for the success of autonomous driving by enabling full detection of the car's surroundings with all relevant objects. Therefore, many motor corporations devote much of their efforts to the research of this part. Automobile company like Ford, IT company like UBER and Google have applied mechanical LIDARs on their prototype autonomous cars, which are now supplied by Velodyne, famous as the roof-mounted spinning coffee can on Google's self-driving cars. For the prototype of Ford autonomous driving car, there are 4 Velodyne 64-beam LIDARs placed on the top of the car, each costs $80,000, so the Lidar sensors cost $320,000 in total just for one car. They work together to detect whole 360 degrees field of view and build a real-time 3D map.

Obviously, the price of LIDAR is one of the key elements that prevents putting autonomous cars on the market. Besides the extremely high price, these traditional appearance are two main reasons why autonomous cars do not become practical. For these limitations, People are considering utilizing electronic components instead of mechanical

parts to implement light beams steering which is also known as the Solid State Lidar. Considering the limitation of field of view of the flat solid state Lidar, we proposed an integration of the vehicle head/ tail lights system with the solid state lidar chip on the four vehicle corners, Which lead to a requirement of at least 90 degree Field of View (FOV) for each lidar to form a whole 360 degree coverage around the vehicle, illustrated in Fig. 1.1. Inspired by this, another concept of using multiple solid state Lidars with a FOV less than 90 on one vehicle can also be a solution to cover full 360 degree detection range.

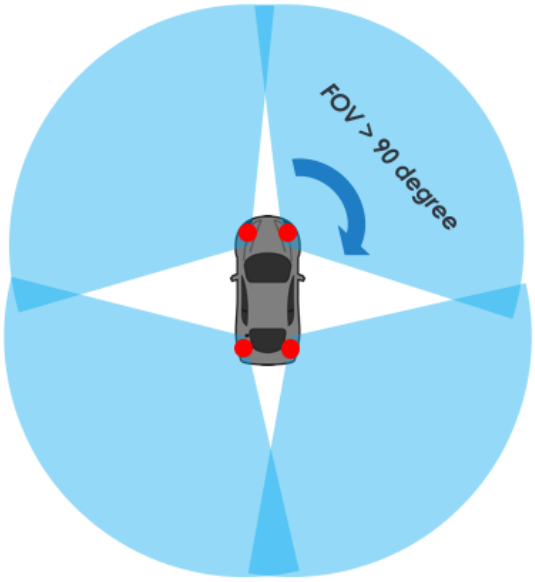

Fig. 1.1 Illustration of using 4 solid state Lidars for full 360 detection

In recent years, with the development of solid-state Lidar (light detection and ranging) systems, groups of research projects utilizing Optical Phased Arrays (OPAs), also known as the surface grating couplers arrays to realize spatial scanning with one or multiple beams generated from a photonic chip [1-7]. The first integrated OPA was presented by Vasey [27] A beam with a width of 0.086 degree was steered over a 0.83 degree range using 43 elements. The performance was limited due to the large element spacing. A typical grating coupler on a silicon-on-insulator (SOI) wafer can be easily fabricated by two-step UV lithography [8], and the coupling efficiency is reported to be up to 93% with different designs [9]. With a high coupling efficiency and an easy fabrication process, the grating coupler has become a promising candidate for achieving the free space coupling of laser beam [10].

1.2 FDTD Simulation Method

Though covering all light's technical applications over the whole spectrum, most photonic applications, such as telecommunications, optical fiber communications, laser emitting are in the range of visible and near-infrared, which is also known as the application in high-frequency EM field. The calculation and analysis of high-frequency EM field and the interactions between sub-wavelength nanostructures and the high-frequency EM field have become a type of important topics regarding the development of modern technologies.

Finite-difference time-domain (FDTD) method is a numerical analysis technique used for modeling computational electrodynamics (finding approximate solutions to the associated system of differential equations), It was first proposed by K. S. Yee in 1966. In the following 20 years, its research progress is slow, but there are some preliminary applications in the field of electromagnetic scattering and electromagnetic compatibility. Since the late 1980s, the FDTD method has become one of the important methods for numerical calculation of electromagnetic fields.

Basically, the FDTD method belongs in the class of grid-based differential numerical modeling methods. The time-dependent Maxwell's equations (in partial differential form) are discretized using central-difference approximations to the space and time partial derivatives [11]. The resulting finite-difference equations are solved in the following strategy: the electric field vector components in a volume of space are solved at a given instant in time; then the magnetic field vector components in the same spatial volume are solved at the next instant in time; and the process is repeated again until the desired steady-state EM field behavior is fully evolved [12].

A computational domain must first be established to implement an FDTD solution of Maxwell's equations. It is simply the physical region (device size in the simulation tool) over which the simulation will be performed. The material of each cell in the computational domain can be any material as long as the permeability, permittivity, and conductivity are specified. A source is then specified once the computational domain and the grid materials are established. In the research of photonics, typically, the source can be one or multiple plane

wave sources, Gaussian beam or dipole sources [13-16]. Since FDTD simulations calculate the E and H fields at all points in the computational domain, the computational domain must be finite to assure its residence in the computer memory. This is achieved by inserting artificial boundaries into the simulation space in many cases. To minimize errors introduced by such boundaries, a number of available highly effective absorbing boundary conditions (ABCs) should be applied to simulate an infinite unbounded computational domain [12]. Most modern FDTD implementations use perfectly matched layer (PML) to implement absorbing boundaries [17-18] instead of using a special absorbing "material".

The FDTD calculation requires that the entire computational domain be gridded, and the grid spatial discretization must be sufficiently fine to resolve both the smallest electromagnetic wavelength and the smallest geometrical feature in the model, in most cases we prefer a grid size smaller than 1/10 of the smallest feature size in the computational domain, thus very large computational domains can be developed, which results in very long solution times. Models with long, thin features (such as single graphene layer), are difficult to model in FDTD because of the large computational domain or excessively tiny grid required. The advantages of using FDTD simulation are listed as following:

- FDTD is a time-domain technique, when using a broadband pulse (such as a Gaussian pulse) as the source, the response of the system over a wide range of wavelengths can be obtained with one single simulation. This is very useful in applications where resonant frequencies are not exactly known, or anytime that a broadband result is desired. This is the main reason for implement FDTD simulation for grating coupler design, for the out-coupling angle is wavelength dependent.

- Since FDTD calculates the E and H fields on all the points in the computational domain as they evolve in time, it can provide real-time displays of the electromagnetic field movement through the structure, which is useful in observing propagation and changes in the EM field.

- A wide variety of linear and nonlinear dielectric and magnetic materials can be easily modeled, which allow the user to specify different materials and structures at all

points within the computational area.

- FDTD method uses the E and H fields directly. Since most modeling applications are interested in the E and H fields, it is convenient and time-saving that no conversions must be made after the simulation has run to get these results.

All the simulation results are generated by a commercial software "OmniSim" by Photon Design. The simulation tool is a HP computing class workstation with 32 CPUs and 256G RAM installed.

1.3 Far-field Calculation

While the FDTD method computes electromagnetic fields within a small spatial region, scattered or radiated far fields can be obtained via near-to-far-field transformations [19].

In photonics, the equation of the near-field diffraction is an approximation of the Kirchhoff-Fresnel diffraction. It is used to calculate the diffraction pattern created by the waves propagate through/ around an aperture or an object from relatively close to the object. Usually, the diffraction pattern in the far field is given by the Fraunhofer diffraction equation. Let's start from the near-field.

The near-field can be specified by the Fresnel number, which is defined as follow:

$$F \triangleq \frac{\alpha^2}{L\lambda}$$

Where α is the size of the aperture, L is the distance between the aperture and the viewing screen, and λ is the wavelength of the incident wave. If $F \geq 1$, the diffracted wave is in the near field, and the Fresnel diffraction integral can be used to calculate its physical property.

Now given the electric field diffraction pattern at point (x, y, z), shown in Fig. 1.1:

$$E(x,y,z) = -\frac{i}{\lambda}\iint_{-\infty}^{\infty} E(x_0, y_0, 0)\frac{e^{-ikr}}{r}\,dx_0 dy_0, \qquad k = \frac{2\pi}{\lambda}$$

$E(x_0, y_0, 0)$ is a scalar field at point $(x_0, y_0, 0)$ in the aperture plane and k is the wavenumber.

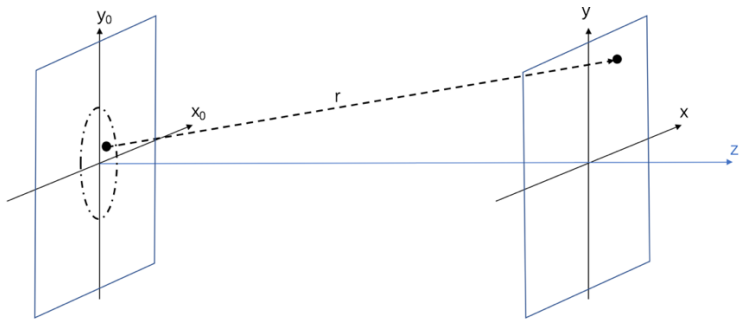

Fig. 1.2 Illustration of the electric field diffraction pattern

$r = \sqrt{(x - x_0)^2 + (y - y_0)^2 + z^2}$ is the distance between point (x, y, z) and $(x_0, y_0, 0)$. To calculate this integral equation, we can first simplify the algebra by substituting $(x - x_0)^2 + (y - y_0)^2$ with ρ^2 , then we have

$$r = \sqrt{\rho^2 + z^2} = z\sqrt{1 + \frac{\rho^2}{z^2}}$$

Using Taylor series expansion: $r = z + \frac{\rho^2}{2z} - \frac{\rho^4}{8z^3} + \cdots$

The key of the Fresnel approximation is to assume that the third term and the terms after it is very small and thus can be ignored. Which means it has to be much smaller than the period of the phase: 2π

$$k\frac{\rho^4}{8z^3} \ll 2\pi$$

$$r \approx z + \frac{\rho^2}{2z}$$

This is so-called the Fresnel approximation and the inequality above is the condition. Substitute the Fresnel approximation into the electric field of the diffraction pattern, we have the Fresnel integral:

$$E(x, y, z) = \frac{ie^{-ikr}}{\lambda z} e^{-ik(x^2+y^2)/2z} \iint_{-\infty}^{\infty} E(x_0, y_0, 0) e^{-ik({x_0}^2+{y_0}^2)/2z} e^{i\frac{k}{z}(xx_0+yy_0)} dx_0 dy_0$$

When the distance z is large, the diffraction pattern is viewed at a long distance from the diffracting object:

$$z \gg \frac{k}{2}\left(x_0^2 + y_0^2\right) \ , \ F = \frac{\alpha^2}{L\lambda} \gg 1$$

The phase term can be ignored and we can have the far-field diffraction pattern, which is also known as the Fraunhofer diffraction:

$$E(x, y, z) = \frac{ie^{-ikr}}{\lambda z} e^{-ik(x^2+y^2)/2z} \iint_{-\infty}^{\infty} E(x_0, y_0, 0)\, e^{i\frac{2\pi}{\lambda z}(xx_0+yy_0)}\, dx_0 dy_0$$

This is simply the Fourier transform of the near-field Fresnel approximation [19]. Analytical solution of this integral is possible for the simplest diffraction geometries. However, for complex structures, it is usually calculated numerically with computer software, such as FDTD simulation tools.

Chapter II

Diffraction Grating theory and Grating coupler

2.1 Basic Model

The typical example of the grating coupler is illustrated in Fig. 2.1. The basic model of the grating coupler has a single periodicity Λ_{gr}. In most studies concentrating on Si-based grating couplers, the device is fabricated on a silicon on insulator (SOI) wafer [1, 2]. A Si layer of 220 nm thickness is first deposited on top of a 2 μm-thick glass layer as an SOI wafer. Then the Si layer is etched to form the rectangular waveguide layout; the next step is to etch a depth of d nm to form the grating structure on the waveguides.

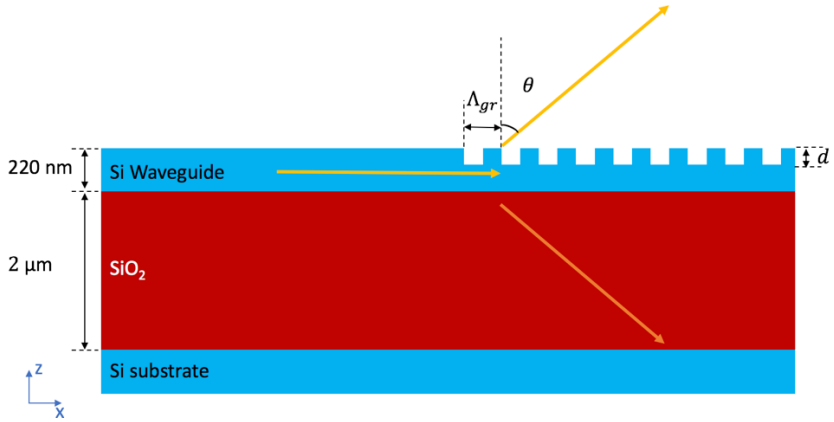

Fig. 2.1 Basic model of the grating coupler

In the simulation software used in the thesis (OmniSim, produced by Photon Design), the computational coordinate was set to be as following: positive x direction is vertical upwards, positive z is the direction of horizontal to the right, while positive y is the direction point out of the screen, therefore, when calculating in 2-dimensions, the neglected components are y components. Since we are more interested in the out-coupling angle in the X-Z plane, 2D simulation would be a better choice in reduce the use of computing power

In our grating coupler cases, to reduce the long solution times, we took more effort on the simulation of the grating area on the waveguide since we are more interested in its beam steering property, the light source (fundamental mode excite) is set to be 20 microns away from the coupling area which has been proven to be long enough for not affecting the far-field angle result in the FDTD simulation. In the reality, the distance between the light source and the coupling area should be far longer than the computational model demonstrated here.

Fig. 2.2 shows the screenshot of the basic model for one beam steering grating coupler in the simulation software. Different material in this model is shown in different color, blue part shows a cross-section of a silicon waveguide with the out-coupling grating area, and the red part shows the 2 μm-thick silicon dioxide layer. The red lines with an arrow in the center are the sensors to calculate the energy follow and far field angle in the direction of the arrow. Yellow line with an arrow in the middle is the symbol of the laser light source. Fig. 2.3 shows the far-field angle distribution of the grating coupler at a wavelength of 1550 nm, calculated using the far-field calculator in the OmniSim software, the direction of the angle is parallel to the waveguide.

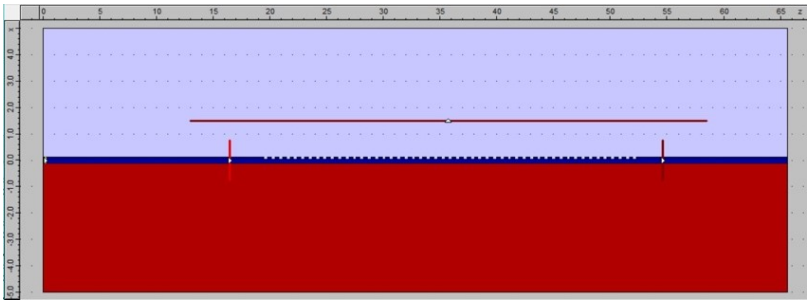

Fig. 2.2 Screenshot of one beam steering grating coupler

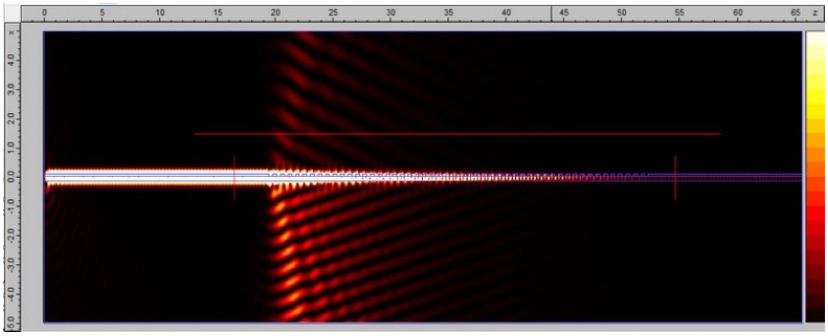

Fig. 2.3 Screenshot of the field distribution

2.2 Coupling Theory

Lots of research has been done in the development of grating couplers, mainly to couple light from optical fibers into integrated photonic circuits [20 –23]. In this work, our main interest is the properties of these gratings while coupling light from the photonic chip into free space. Due to the periodic nature of diffraction, constructive interference will occur in certain directions, described by the grating equation. At the very beginning, the waveguide thickness is chosen such that it will only support a single mode.

While the wavelength at 1.55um is the most common wavelength using in the optical communication, silicon is chosen as the waveguide material for the advantage of easy fabrication, low cost and low loss for the wavelength of 1.55um. 220nm is set as the waveguide thickness to fulfill the single mode condition at the same time.

2.2.1 Geometrical Theory

The ray optics to determine the condition for two rays reflected off the grating area to constructively interfere at an angle θ. This is usually an easier way to understand the grating coupler, let's zoom in the grating area of the grating coupler introduced before, we choose the grating periodicity as Λ_{gr} , such that the path length difference (a) results in constructive interference between Ray 1 and Ray 2.

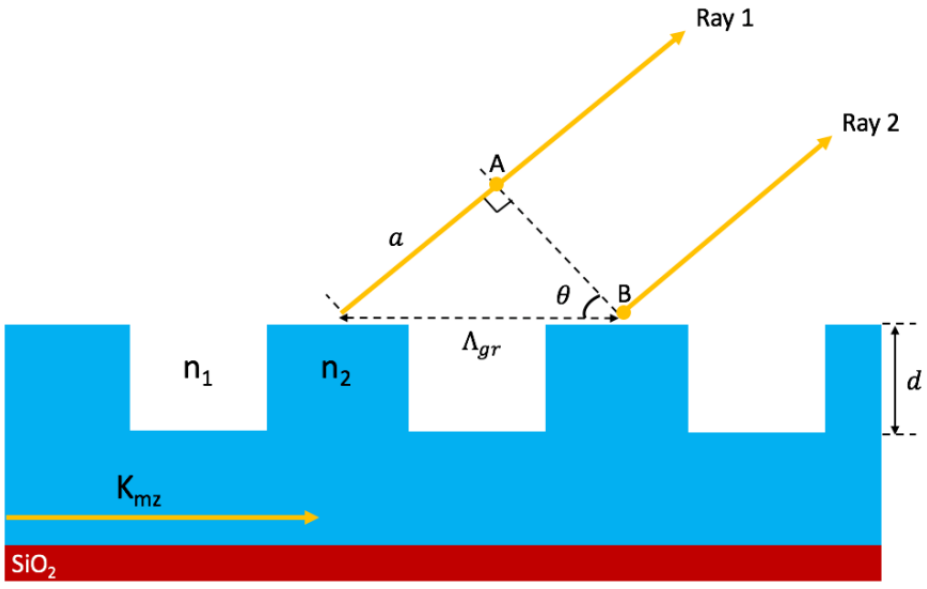

Fig. 2.4 Illustration of beam coupling mechanism

The Fig 2.4 shows the constant phase wavefronts, normal to the direction of propagation, the wavefront at B point overlaps the wave front at point A. The two rays interfere with each other unless the wavefront A on ray 1 is in phase with the wavefront at B on ray 2, the two would destroy each other [35]. Only certain out-coupling angles θ give rise to the constructive interference and hence only certain angles can exist in the air. For the phase match condition:

$$k_{mz}\Lambda_{gr} - k_1 a = 2\pi m, \quad m = 0, \pm 1, \pm 2 \ldots$$

k is the propagation constant, given by $2\pi/\lambda$, where λ is the wavelength inside the material. We use n_{eff} as the effective index of refraction of the mode in the waveguide, here the only mode inside a 220nm waveguide is the fundamental mode. The equation can be derived as:

$$\frac{2\pi}{\lambda} n_{eff}\Lambda_{gr} - \frac{2\pi}{\lambda} n_1 a = 2\pi m$$

$$n_{eff}\Lambda_{gr} - n_1 a = m\lambda$$

$$n_{eff}\Lambda_{gr} - \mathrm{n}_1\Lambda_{gr}\sin(\theta) = m\lambda$$

$$\sin(\theta) = \frac{m\lambda - n_{eff}\Lambda_{gr}}{-n_1\Lambda_{gr}}$$

$$\sin(\theta) = \frac{n_{eff} - \dfrac{m\lambda}{\Lambda_{gr}}}{n_1}, \qquad m = 0, \pm 1, \pm 2 \ldots$$

2.2.2 Bragg Theory of Periodic Media

First, when a uniform wave traveling through a dielectric object, a portion of wavefront will be delayed after traveling through a dielectric object, the fields are perturbed by the objects, shown in Fig. 2.5(a) If we have a periodic array of those objects, the fields get perturbed and comes out with a perturbation that takes on the exact same symmetry as the structure that let it in.

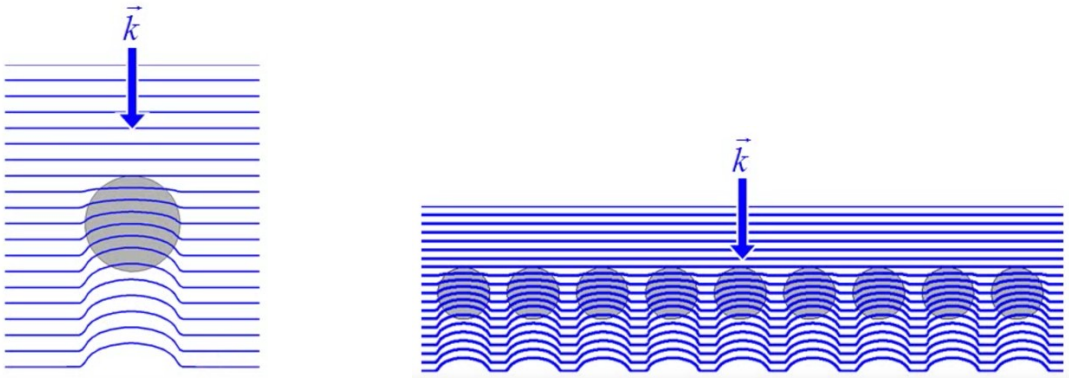

(a) (b)

Fig. 2.5 Electric fields perturbed by structures (a) Single dielectric structure; (b) Periodic structures

As discussed above, the diffraction gratings can be characterized by their grating vector $\boldsymbol{K}$, a grating vector is very much like a wave vector in that its direction is normal to planes and its magnitude is 2π divided by the spacing between planes. When the grating is wide (for example in the y-direction of Fig. 2.5(b), the problem is actual a 2D problem, the structure with such a grating period of Λ_{gr}, the grating k-vector can be described as:

$$\boldsymbol{K} = \frac{2\pi}{\Lambda_{gr}} \boldsymbol{s}_x$$

Here, $\boldsymbol{s_x}$ represents the unit vector along the x-direction. Since there is no periodicity in the z-direction, there is a continuum of grating k-vectors that can be added in the z-direction. The magnitude of the grating vector $|\boldsymbol{K}| = \frac{2\pi}{\Lambda_{gr}}$

The Bragg condition for periodic media, also known as the Floquet condition, dictates that the k-vector of each diffracted order $\boldsymbol{k}_{out,m}$ from a periodic medium simply equals the sum of the k-vectors of the incident light $\boldsymbol{k}_{inc}$ (un-diffracted transmitted wave) with an integer m multiples the grating vector of the periodic medium $\boldsymbol{K}$:

$$\boldsymbol{k}_{out,m} = \boldsymbol{k}_{inc} - m\boldsymbol{K}$$

where m=0, $\pm 1, \pm 2, \ldots$ i.e. while m=1, and the $\boldsymbol{k}_{out}$ in this equation means the wave vector of the 1st diffracted order. And the infinite sets of resulting wave vectors are known as Floquet waves. Although the set of Floquet waves contains an infinite number of diffracted orders, only certain of those orders can exist physically.

To explore further, the Bragg condition here can be derived from the periodic permittivity of the grating structure [30 - 32]. Let's think about the field inside the periodic structure, to simplify, we start with the plane wave and sinusoidal grating as an example here.

$$E(\vec{r},t) = E_0 \cos(\omega t - \vec{k}\cdot\vec{r} + \varphi_0)$$

Apply Euler's formula, and Simplified: $E(\vec{r}) = E_0 \cos(-\overrightarrow{k_{inc}}\cdot\vec{r}) = E_0 \cdot \mathcal{R}e\left\{e^{-j\overrightarrow{k_{inc}}\cdot\vec{r}}\right\}$

A wave propagating through this grating takes on the same symmetry, consists of two terms, an amplitude term and a plane wave phase term. This plane wave phase term does not take on the symmetry of anything other than a plane wave traveling of some arbitrary direction. Actually, it is the amplitude envelop of that wave takes on the same symmetry as the structure that the wave exists. So, the total field is the product of these two.

$$E(\vec{r}) = A(\vec{r})e^{-j\overrightarrow{k_{inc}}\cdot\vec{r}}$$

Then, we can express the grating in general, we have a grating vector $\vec{K}$, $\cos(\vec{K}\cdot\vec{r})$ give out the generic unit amplitude, thus, $\Delta\varepsilon\cos(\vec{K}\cdot\vec{r})$ is the dielectric contrast of the grating. Add up this term to the average dielectric constant, we can have the dielectric function of a sinusoidal grating, the dielectric function of a sinusoidal grating can be written as:

$$\varepsilon_r(\vec{r}) = \varepsilon_{r,avg} + \Delta\varepsilon\cos(\vec{K}\cdot\vec{r})$$

We can derive the field inside the grating as:

$$E(\vec{r}) = A(\vec{r})e^{-j\overrightarrow{k_{inc}}\cdot\vec{r}}$$

$$= A\left[\varepsilon_{r,avg} + \Delta\varepsilon\cos(\vec{K}\cdot\vec{r})\right]e^{-j\overrightarrow{k_{inc}}\cdot\vec{r}}$$

$$= A\,\varepsilon_{r,avg}e^{-j\overrightarrow{k_{inc}}\cdot\vec{r}} + \frac{A\Delta\varepsilon}{2}e^{-j(\overrightarrow{k_{inc}}-\vec{K})\cdot\vec{r}} + \frac{A\Delta\varepsilon}{2}e^{-j(\overrightarrow{k_{inc}}+\vec{K})\cdot\vec{r}}$$

Now, a single wave has been split into three waves due to the grating, one in the original direction and two directions on either side of the central direction. Each of those waves can be split into three waves as well, and then goes on to infinity.

$$e^{-j\overrightarrow{k_{inc}}\cdot\vec{r}} \rightarrow \begin{cases} e^{-j\overrightarrow{k_{inc}}\cdot\vec{r}} \\ e^{-j(\overrightarrow{k_{inc}}-\vec{K})\cdot\vec{r}} \\ e^{-j(\overrightarrow{k_{inc}}+\vec{K})\cdot\vec{r}} \end{cases} \quad e^{-j(\overrightarrow{k_{inc}}-\vec{K})\cdot\vec{r}} \rightarrow \begin{cases} e^{-j(\overrightarrow{k_{inc}}-\vec{K})\cdot\vec{r}} \\ e^{-j(\overrightarrow{k_{inc}}-2\vec{K})\cdot\vec{r}} \\ e^{-j\overrightarrow{k_{inc}}\cdot\vec{r}} \end{cases} \quad e^{-j(\overrightarrow{k_{inc}}+\vec{K})\cdot\vec{r}} \rightarrow \begin{cases} e^{-j(\overrightarrow{k_{inc}}+\vec{K})\cdot\vec{r}} \\ e^{-j\overrightarrow{k_{inc}}\cdot\vec{r}} \\ e^{-j(\overrightarrow{k_{inc}}+2\vec{K})\cdot\vec{r}} \end{cases} \quad \dots$$

In conclusion, the wave vector of the possible diffract mode is given by:

$$\vec{k}_{out,m} = \vec{k}_{inc} - m\vec{K} \qquad m = \infty, \dots, -2, -1, 0, 1, 2, \dots, \infty$$

This equation describes the total set of allowed harmonics inside the grating, which is also known as the Bragg condition [33]. We can see the potential to have an infinite plane wave traveling in all different directions. Now, we can consider what will happen when a light wave on the incident to a grating, shown in Fig. 2.6

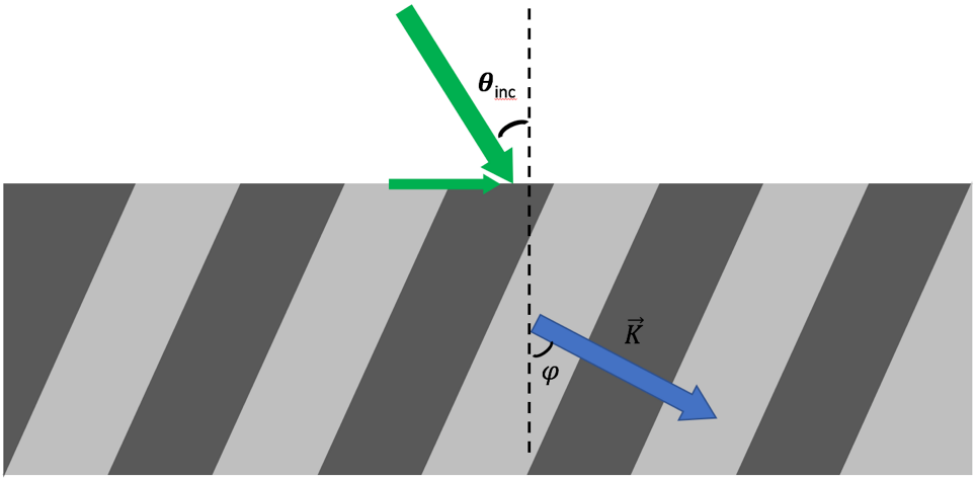

Fig. 2.6 Illustration of light on the incident to grating structures

The boundary conditions required the tangential component of the wave vector to be continuous. The transverse component travels across the interface should also be continuous. So, while the wave is entering a grating, it had to be expanded to all the possible transverse wave vectors that can exist in the grating. In the x-direction inside the grating, the phase matching condition:

$$k_{x,m} = k_{inc} - mK_x$$

The longitudinal vector component is calculated from the dispersion relation:

$$k_{z,m}^2 = (k_0 n_{avg})^2 - k_{x,m}^2$$

For large m, $k_{z,m}$ can become imaginary, which indicates that the highest order spatial harmonics are evanescent.

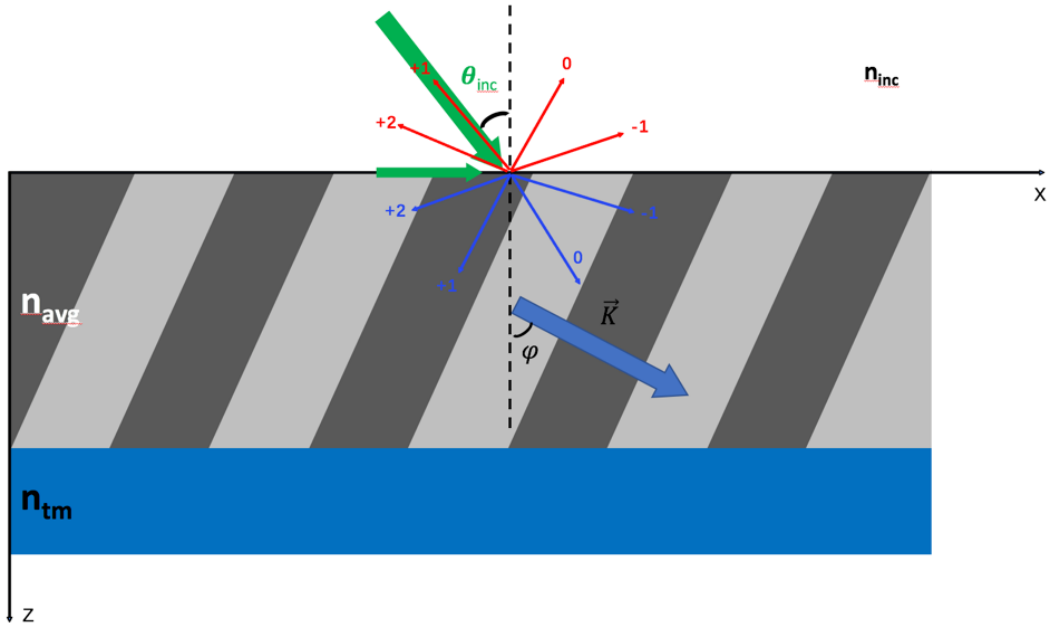

Fig. 2.7 Reflection and transmission modes in the grating structure

$$k_{x,m} = k_{inc} - mK_x$$

$$k_0 n_{avg} \sin\theta_m = k_0 n_{inc} \sin\theta_{inc} - m\frac{2\pi}{\Lambda_x}$$

$$\frac{2\pi}{\lambda_0} n_{avg} \sin\theta_m = \frac{2\pi}{\lambda_0} n_{inc} \sin\theta_{inc} - m\frac{2\pi}{\Lambda_x}$$

$$n_{avg} \sin\theta_m = n_{inc} \sin\theta_{inc} - m\frac{\lambda_0}{\Lambda}\sin\varphi$$

We have derived the general grating equation base on the Bragg condition and the boundary condition [34]. For the reflection region, we can directly replace the n_{avg} with n_{ref} (same as n_{inc}). For the transmission region, the n_{avg} can be replaced as n_{tm} with the same reason. While applying this equation into our grating coupler, the light is incident from the waveguide and perpendicular to the grating structure, $\varphi = 90°$. We use n_{eff} as the average refractive index of the whole waveguide and grating area, and out-coupling area where we are most interested in is the air, n_{inc}=1, Fig. 2.7 Thus, the grating equation of the grating coupler can be simplified as:

$$n_{air}\sin\theta_m = n_{eff}\sin 90° - m\frac{\lambda_0}{\Lambda}\sin 90°$$

$$\sin\theta_m = n_{eff} - m\frac{\lambda_0}{\Lambda} \qquad m = 0, \pm1, \pm2, \ldots$$

2.2.3 K-Space Diagram

Another approach to look at these grating couplers is by using the k-vector diagram, a way of solving Bragg theory with periodic media graphically [20]. The k-vector diagram explains the reflection and transmission of the incident light due to the periodic grating structures. This kind of diagram use the concentric circles with different radius to indicate the magnitude of the wave vector k in different materials [21-22]. And the grating structures are modeled as the center of these circles. The angle of the rays travels away from the center of the circles indicate the direction of propagation, and its magnitude equal to the magnitude of the wave vector, Fig. 2.8. With the k-vector diagram, the Bragg condition can be easily represented by adding multiples of the grating vector to the un-diffracted wave vector of the transmitted field by the head to tail method. The next step is to draw the Floquet addition of the reflected and transmitted waves in the incident and transmitted mediums, which is done by applying the boundary conditions for electric fields, also known as phase matching [23]. We can explain phase matching graphically by drawing sets of lines that pass through the head of each Floquet wave vector and are perpendicular to the boundary between the incident and transmitted mediums. Only the intersections of these lines with the circles are then viable solutions. Thus, the diffracted wave vectors start at the center of the circle, and end where the vertical lines of the matched phase crossover with the circles.

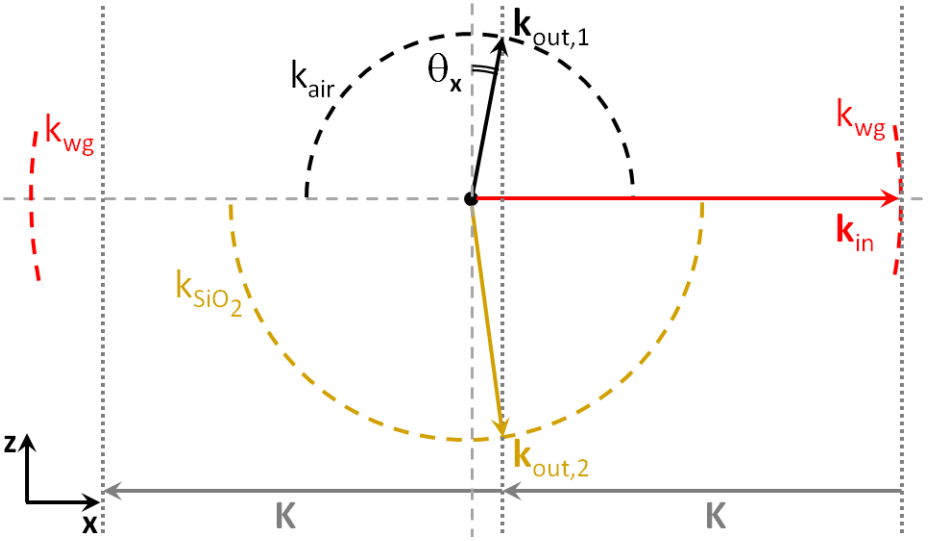

Fig. 2.8 Illustration of a K-space diagram

Fig. 2.8 shows that, in this configuration, the grating coupler produces free space coupling. Such a k-vector diagram drawn to scale for a grating period of 650 nm. This is one of the periods used for the grating coupler throughout this work. The incident light, traveling in the positive x-direction, feel an average effective index of the fundamental mode in the grating area of the silicon waveguide and the periodic structure n_{eff}. This effective index is only used for the light traveling inside the waveguide, which is in the positive or negative x-direction in the k-vector diagram. The magnitude of the wave vector inside the grating is denoted by k_{wg}. The diffracted light that is coupled upwards into the air meet an index of air (n_{air}=1), therefore a circle with dotted lines is drawn with radius k_{air}, being the size of a wave vector in air. While the diffracted light coupling downwards into the glass (n_{sio2}=1.44) and therefore a circle with yellow dotted lines is drawn with the radius of k_{sio2}.

To find the diffracted light directions, we need to add an integer times the wave vector of the grating, denoted as **K**, while we can add any k-vector in the z-direction. Therefore, vertical lines are drawn in Fig. 2.8, spaced a distance K in the x-direction. The diffracted light should meet the boundary conditions and lie on one of these lines. In this example (650nm), we can see one beam diffracted upwards, $\mathbf{k}_{out,1}$ and one beam diffracted downwards $\mathbf{k}_{out,2}$. Such a k-vector diagram gives clear insight in what direction light can be diffracted.

In general, as the grating period decreases, the angles of the out-coupling beams increase until they are cut off. Two special conditions can be observed in this discussion, if the grating structure diffracts the light into the opposite direction of the incident light inside the wave guide, we usually call this kind of device a Bragg grating. Only one solution can be found to fit the Bragg condition when the k-vector is twice the k-vector in the incident light $\mathbf{k}_{in}$. This is usually called the first order Bragg grating, which is normally used in the optical fibers as filters.

$$|\boldsymbol{K}| = 2|\boldsymbol{k_{in}}|$$

$$\frac{2\pi}{\Lambda_{gr}} = 2n_{eff}\frac{2\pi}{\lambda}$$

$$\Lambda_{gr} = \frac{\lambda}{2n_{eff}}$$

When the grating vector equals to the k-vector of the incident light $\mathbf{k}_{in}$, known as a second-order Bragg grating coupler, as its name, the second order of the diffracted light propagates back in the opposite direction of the incident light in the waveguide. Therefore, this kind of structure can achieve guided mode coupling between a forward traveling wave and a backward traveling wave, the grating period is equal to the free space wavelength of the light divided by the effective index of the guided mode. This discussion has shown that free space coupling is achievable with these grating couplers, by adjusting the grating and waveguide parameters, chip to chip coupling and guided mode coupling are also achievable.

2.3 Tunable Parameters for Beam Steering Application

We have introduced several theories in the grating coupler. From the grating equation derived above, it is easy to tell that the out-coupling angle θ is related with the effective index of the grating area n_{eff}, the wavelength of the laser source λ in vacuum, the period Λ_{gr} of the grating structure, and the background refractive index n_{bg}. However, for the application of solid-state Lidar, the interested out-coupling area (background) is usually air where n_1 is set to be 1 in the simulation. In reality, while using OPAs as the beam steering elements in solid state Lidar, correction parameters for the background will be added for precise detection.

For the tunable parameters listed here, there will be two approaches for changing the beam angle. Which we can separate them into passive and active structures. Passive structure means the properties of the structure itself won't change, all the result is controlled by the source or the wavelength change. Active, as its name says, some characteristic of active material will be utilized in the grating structure, which means the effective index of the refraction in this material can be controlled by voltage, pressure or temperature, etc.

It seems like we have already known everything about the direction of the diffraction angle of this structure. However, the grating equation only predicts the direction of the diffracted mode, not how much energy is in them. The out-coupling energy and beam quality are also important while applying this structure to the application of beam steering in the solid-state Lidar. We must obtain a rigorous solution to Maxwell's Equations to determine the

amplitude and polarization of the diffracted mode, which will be solved by the FDTD simulation software [35-36].

Chapter III

One beam steering

3.1 3D Simulation Results

At the very beginning, the grating coupler for the application of solid-state Lidar is set to be a 3D model with the width of 4um in the y-direction. Screenshot of the 3D model is shown in Fig. 3.1 The grating has a fill factor of 0.5 and the periodicity is set to be 650 nm, the etching depth is 70nm. These are the typical parameters using in the optical communication for 1550nm light coupling, for example, couple 1550nm light into an optical fiber [20].

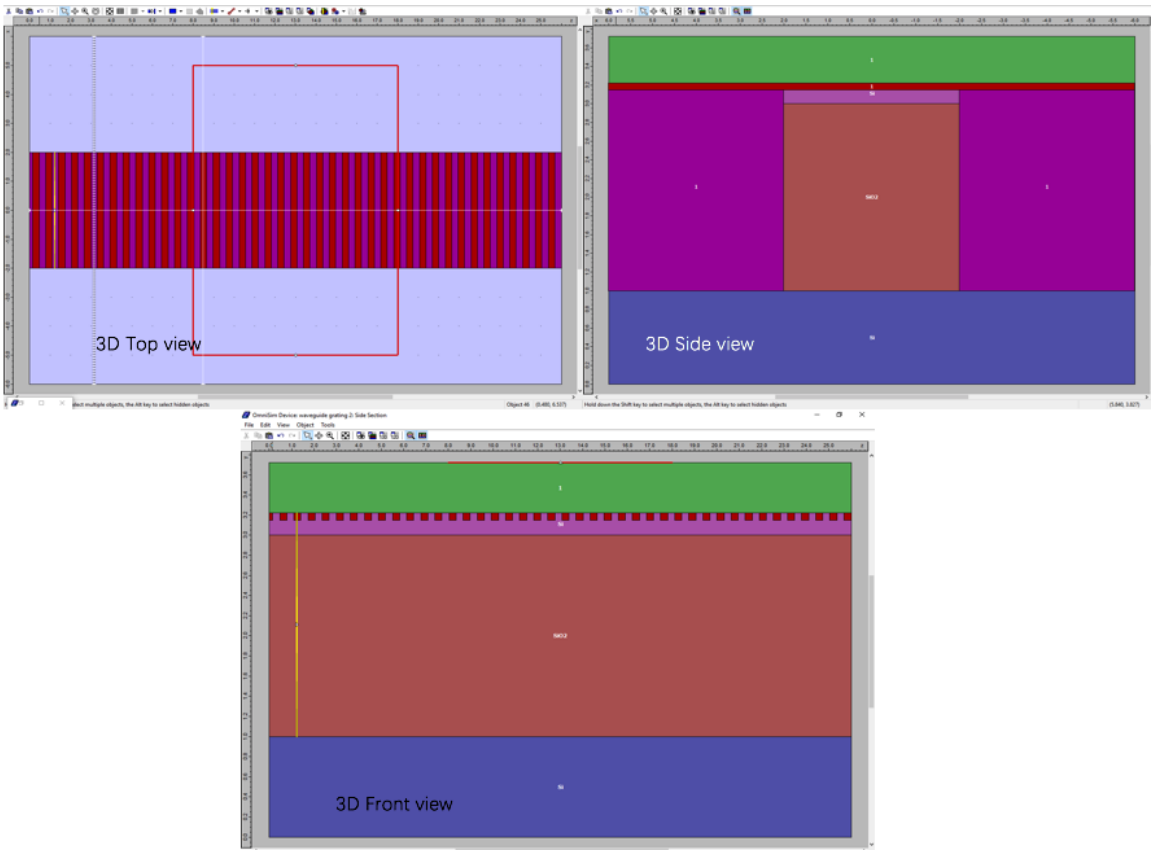

Fig. 3.1 Illustration of the grating coupler 3-D model

A far-field sensor is placed on the top of the grating structure to calculate the normalized out-coupling angle, both TE and TM mode are simulated in this structure. This is, obviously,

a passive structure, all the other parameters include periodicity, fill factor and etching depth are fixed in this group of simulations. The input wavelength is tuned to change the out-coupling beam angle at 1.5 microns, 1.55 microns, and 1.6 microns. The normalized out-coupling beam angle is shown in Fig. 3.2

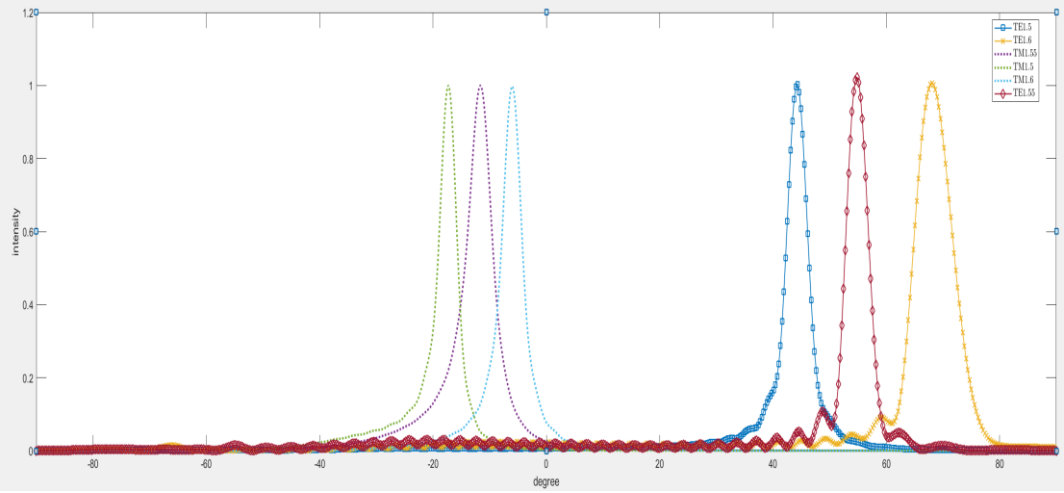

Fig. 3.2 Normalized out-coupling angles

We can have a conclusion that out-coupling beam angle increased with the wavelength. The simulation results match the theoretical prediction very well, and for this structure, TM mode has a better resolution while TE mode gives a larger range of 24 degrees, but all the simulations are too time-consuming and drained too much computing power from the workstation. To calculate the out-coupling angle for one wavelength in this 3D model will take the full computing power of the workstation for more than 5 hours. Thus, 3D simulation is not suitable for design and structure optimization.

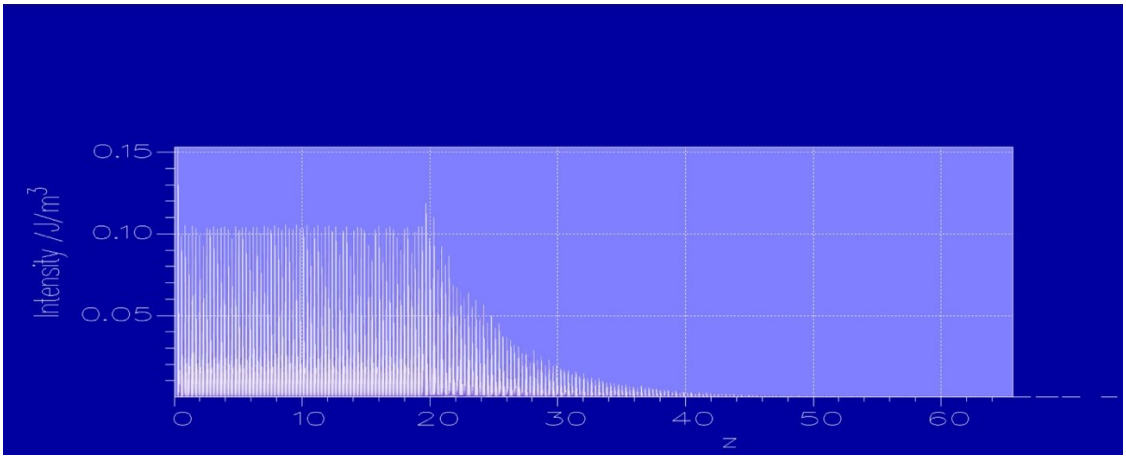

Fig. 3.3 The electric field distribution near the grating area

The electric field near the grating area has also been simulated, the result is shown in Fig. 3.3 It shows the typical behavior of the magnitude of the electric field that is coupled into the air is an exponential decay. The decay length of approximately 6-7 um is related to the difference of the effective index of the grating elements. With a very shallow etch, the difference of the grating elements will be smaller, thus, the decay length will be longer. Because it is the size of the radiation aperture who decide the out-coupling beam width, design in the etching depth can be a way of controlling the beam width.

3.2 Wavelength Tuning and Color Map

For 2D simulations, the field in y dimension will not be considered and calculated. Since we are more interested in the out-coupling, 2d results won't be an issue for the out-coupling angle which is in the x-z plane, this can also be proofed in the next analysis.

2D model also shows the side cross-section of a typical SOI-based grating coupler, it contains a 220 nm-thick Si waveguide on top of a glass layer with a thickness of 2μm. The Si layer of 220 nm is then etched to form the waveguide layout.

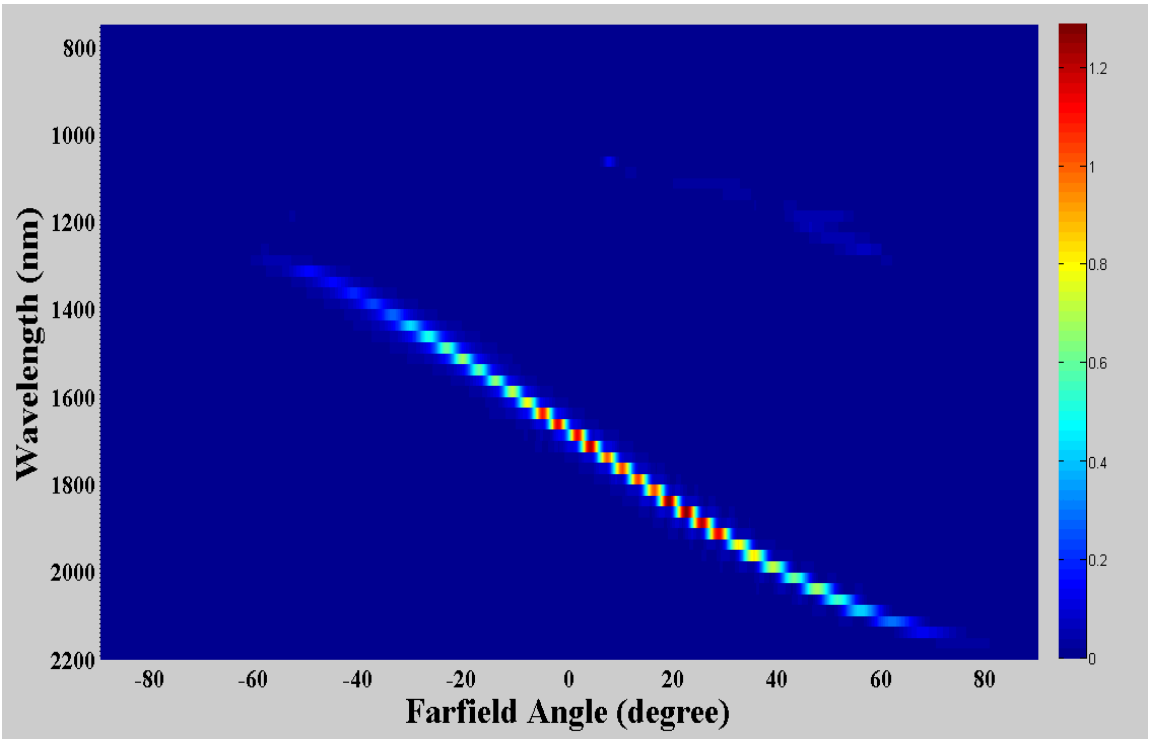

Fig. 3.4 Wavelength tuning map for single beam steering

To complete the wavelength tuning map for this structure, the parameters for the grating area are set as follow: a grating periodicity of 650nm, fill factor 0.5, 50 periods, 70nm etch depth to match the simulation condition in the X-Z plane of the 3D model. The complete tuning map is shown in Fig. 3.4, the wavelength of the incident source is continuously tuned from 1250 to 2200 nm, the beam coupled into the air turn out to cover a field of view of approximately 130 degree. In the wavelength range of 1700 nm to 2000 nm, the out-coupling beam has the highest intensity and covers an out-coupling angle range of -15 to 25 degree.

All the analysis for the grating coupler in the next chapters are using 2D model as the default configuration.

3.3 Effect of Grating Period Size

We now go further into the effects of the grating period on output coupling. This discussion follows the same configuration of the grating coupler which is already introduced in chapter 2. Fig. 3.5 shows an example of the grating coupler 2D model with a periodicity of 650 nm. For this analysis, we set the thickness of the silicon waveguide as 220 nm, and the refraction index of the silicon layer is 3.477.

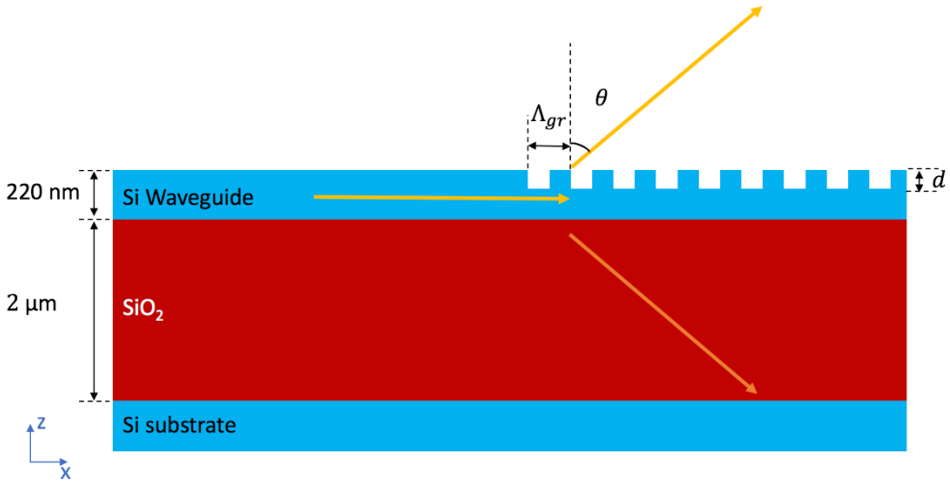

Fig. 3.5 Illustration of 2D grating coupler with a periodicity of 650 nm

Before we go deep into the optimization of the grating coupler, we need to choose a range for the period of the grating. Ideally, we need only one diffracted order coupled into the air. This requests a maximum on the grating period for the coupler. For out-coupling beam, the diffraction equation is derived as:

$$\sin(\theta) = \frac{n_{eff} - \frac{m\lambda}{\Lambda_{gr}}}{n_1}, \qquad m = 0, \pm 1, \pm 2 \ldots$$

We would like the orders higher than m=1 to be cut off. Substituting m=2 into the equation and solve for the period of the grating Λ_{gr} , We can derive the following inequality of the maximum periodicity.

$$\Lambda_{gr} < \frac{2\lambda}{n_{eff} + n_1} \ or \ \Lambda_{gr} > \frac{2\lambda}{n_{eff} - n_1}$$

To ensure the first order will exist in the background area, substitute m=1, we can expand the equation into the following inequality:

$$\frac{\lambda}{n_{eff} + n_1} < \Lambda_{gr} < \frac{\lambda}{n_{eff} - n_1}$$

Although we can derive the condition for the grating period to fulfill the out-coupling condition of the first order, we still need the help of the simulation tool to calculate the effective index of the refraction in the waveguide.

Before using the FDTD simulation tool, we would like to give a rough estimation of the workable period range. We assumed that the refractive index of the grating area is the average refractive index of the teeth (n_2=3.477) and the spacing (n_1=1) part, which is around 2.24. For this analysis, we also assume the effective refractive index of the fundamental mode of silicon waveguide part (without the grating structure part) is around 2.8-2.9, the same as the effective refractive index of slab silicon waveguides with both top and bottom claddings are oxide (n = 1.444) and the refractive index for index is chosen as 3.477 for the wavelength of 1550 nm. With all these assumptions, the effective index of the grating coupler is in the range of 2.24 to 2.9, we use the median 2.58 to substitute in the inequalities above.

$$\Lambda_{gr} < 868\ nm \ \text{ or } \ \Lambda_{gr} > 1975\ nm$$

$$435\ nm < \Lambda_{gr} < 987\ nm$$

The range of the workable period for the input wavelength of 1550nm will be approximately between 435 nm to 868nm. After the FDTD simulation, the far-field results are listed in Fig. 3.6

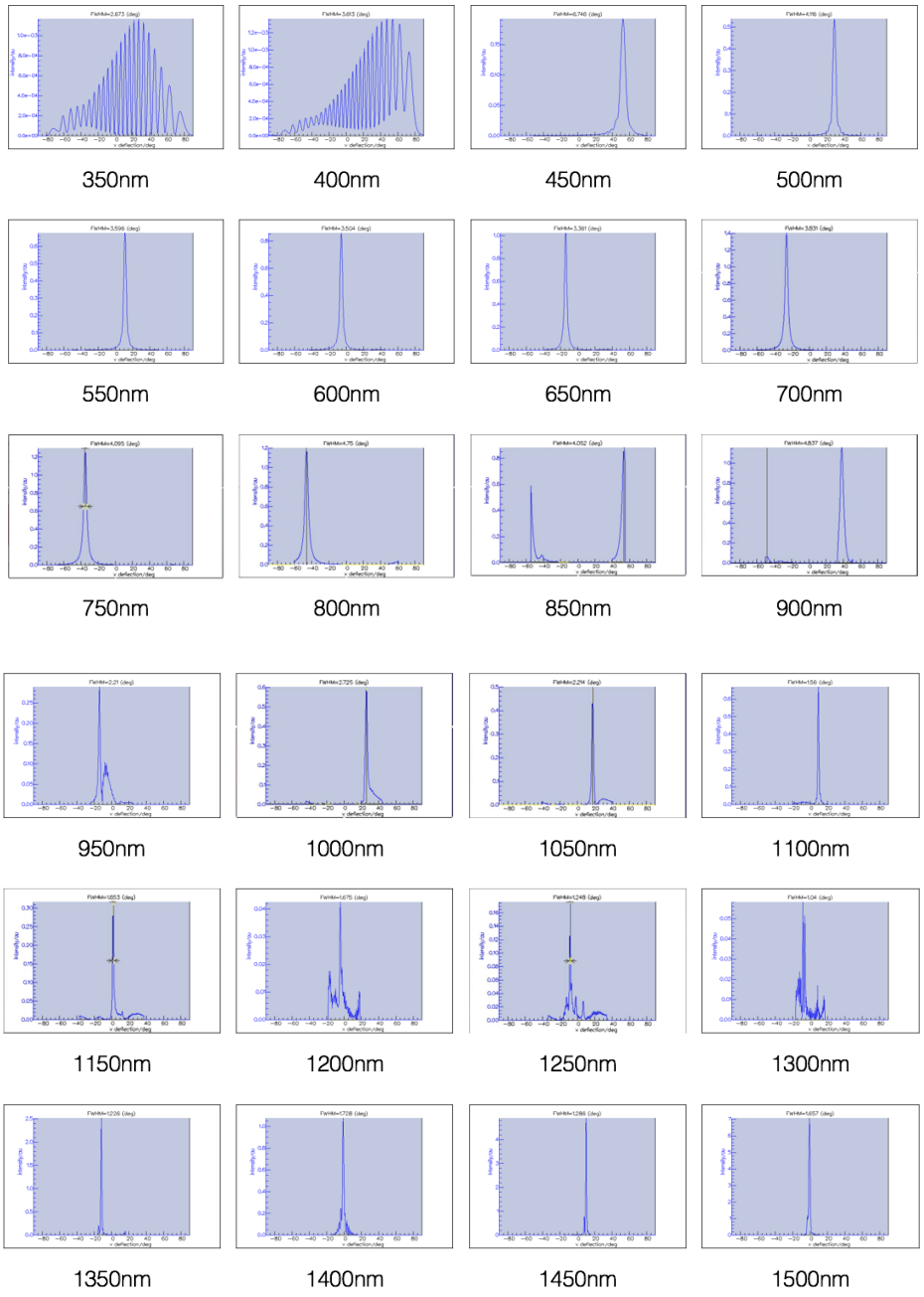

Fig. 3.6 Far-field simulation results with different periodicities

For the first two results, there is no clear out-coupling beam shown. This is already predicted by analyzing the grating equation, for some very small periodicity, the mode is evanescent not diffracted, thus, no out-coupled beam will be detected. An interesting finding is that at the periodicity of 850nm, the simulation result shows two out-coupling beams at the

same time. Which means more than one diffracted modes are coupled into the air. This can also be explained by the grating equation or the K-space diagram, some special periodicity (estimated 868 nm ~ 987 nm) at the input wavelength of 1550nm can make the equation work with different order m at the same time, Fig. 3.7

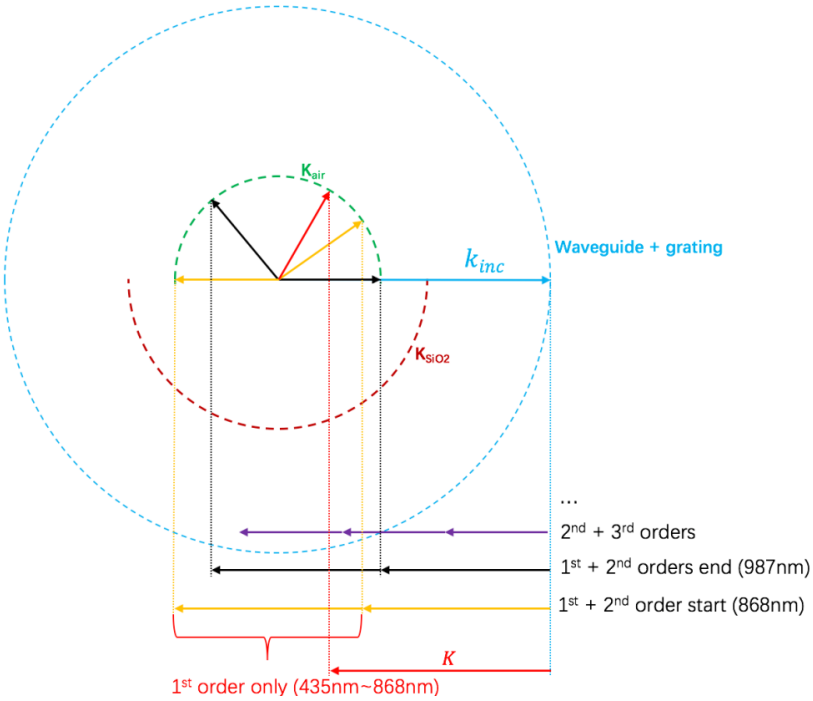

Fig. 3.7 K-space diagram of multiple out-coupling diffracted modes

Note that for the different diffracted mode into the air, the effective index of refraction is not always the same, however with the same fill factor of 0.5, the change of periodicity will not affect much on the effective index of refraction, Fig. 3.8 shows the grating period vs. out-coupling angle of the largest mode being coupled into the air.

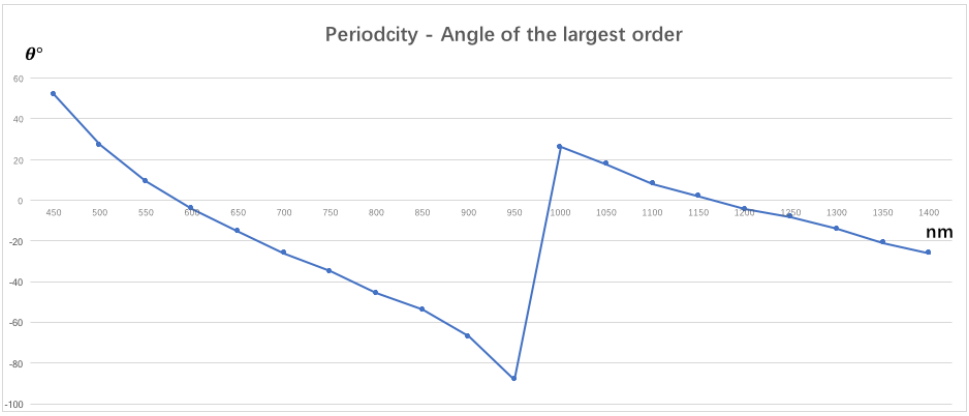

Fig. 3.8 Grating periodicity vs. Angle of the diffracted order with the highest intensity

From Fig. 3.8, we can observe a clear beam out-coupling at the angle of 52.44 degree starting with the grating period of 450nm. At the wavelength of 1550nm, having a period range from 450 to 850nm, the 1st diffracted mode is coupled into the air and can continuously cover an out-coupling range of 134.5 degree.

We can also observe that the out-coupling energy can be varied with different periodicity. As discussed before, the grating equation can just proof the out-coupling angle is related with the wavelength, how the intensity can be affected by the wavelength need more research by using the FDTD simulation tool. Fig. 3.9. shows the complete period tuning map. We have optimized the etching depth to 40nm at the wavelength of 1550nm and all the other parameters have remained the same.

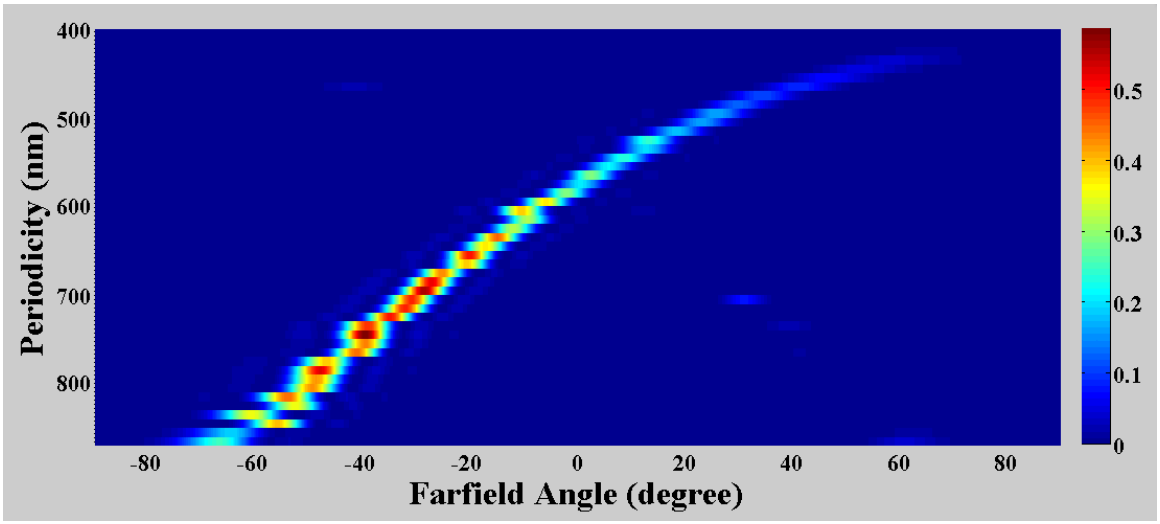

Fig. 3.9 Periodicity tuning map at a fixed input wavelength of 1550 nm

3.4 Research on the Number of Periods

To study the effect of the number of periods on far-field pattern, the periodicity used in the simulation is fixed at 550nm, 650nm and 750nm, as the simulation results shown in the previous chapter, with a periodicity in the range of 450 - 850 nm, the beam coupled into the air is usually the first diffracted order. We set the same simulation condition as before (sinusoidal pulse with the center wavelength of 1550nm) to make sure the new simulation results is only affected by the number of periods. All the other parameters for the waveguide

and grating structure is also fixed except for the number of periods. The number of periods is set to be 5, 10, 30 and 50. The far-field results are shown in Fig. 3.10.

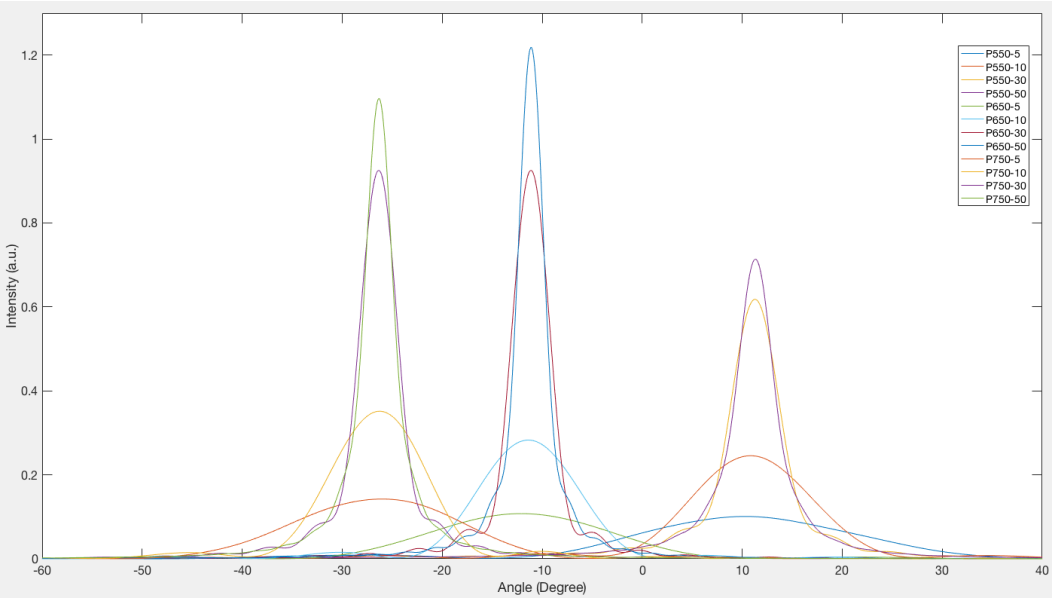

Fig. 3.10 Effect of the number of total periods on beam quality

By comparing the far-field results of different number of periods, the out-coupling intensity decreased as the period number decreased. However, the angle of the out-coupling beam doesn't change much, which in other words, the effective index of refraction won't change much because of the change of period number. There are very small fluctuations on the out-coupling angle, these small fluctuations are acceptable because of the little difference in the effective index of the grating area caused by the period number and calculation error.

The Full Width of Half Maximum (FWHM) also reflect the quality of the out-coupling beam, smaller FWHM usually means better beam quality. It is clearly shown in Fig. 3.10, with a larger number of periods, the FWHM becomes smaller.

While designing the grating area in the application of solid-state Lidar, how the out-coupling beam can be detected should be considered, the beam with higher output energy and beam quality can be detected easier. However, for the data processing (signal filtering), the ideal situation is that the energy of the out-coupling beams is similar to each other regardless of the out-coupling angle. It seems like there is a tradeoff in between base on the results above. In another word, when our interest is designing the out-coupling angle, we can set smaller total number of periods to save the computing power.

3.5 Optimization of Etching Depth

Although, from the famous grating equation, etching depth and the number of periods have little effect on the effective index and thus won't affect much on the out-coupling angle. To understand the effect of etch depth and period number on the coupling efficiency, we performed 4 groups of simulations, groups are separated by etching depth into 40nm, 50nm, 60nm, 70nm, the periodicity of 650nm as the fixed parameter in this part. The thickness of the silicon waveguide on insulator (glass) is set as before, 220 nm on a $2\mu m$ glass wafer.

We already have the prediction that the electric field near the grating area will have a longer decay length with a shallow etching depth [37-40], thus, the out-coupling beam width will be larger. Furthermore, we have already made the conclusion on the larger number of periods will form an out-coupling beam with better quality in chapter 3.2 [41-42]. The number of periods is also tuned here to make complete tables for the use of further engineering design, shown in Fig 3.11 – Fig 3.14. Engineering on the etch depth can increase the out-coupling efficiency are also reported [43-44].

Depth=40, theta=-20.2	Intensity (a.u.)	fwhm (degree)	Transmission(a.u.)
N=5	0.057954	21.8708	0.73634
N=6	0.077460	18.6281	0.69677
N=7	0.101000	16.2150	0.66320
N=8	0.120587	14.7765	0.63002
N=9	0.146869	13.1860	0.59426
N=10	0.175813	11.8987	0.56506
N=11	0.199634	11.0541	0.53344
N=12	0.231872	10.1207	0.50363
N=13	0.263431	9.3755	0.47948
N=14	0.292388	8.7794	0.45188
N=15	0.329221	8.1732	0.42878
N=16	0.361294	7.7277	0.40886
N=17	0.394981	7.2926	0.38596
N=18	0.434381	6.8689	0.36745
N=19	0.465740	6.5818	0.35005
N=20	0.502790	6.2581	0.33039

Fig 3.11 Effect of etching depth on beam quality (Depth 40 nm)

Depth=50, theta=-16.6	Intensity (a.u.)	fwhm (degree)	Transmission(a.u.)
N=5	0.067153	20.9815	0.70752
N=6	0.088609	18.1806	0.67942
N=7	0.109448	16.0891	0.63923
N=8	0.138458	14.0261	0.59918
N=9	0.166896	12.6476	0.57293
N=10	0.190999	11.7346	0.54143
N=11	0.224105	10.6431	0.50546
N=12	0.259135	9.7816	0.48139
N=13	0.287108	9.1974	0.45523
N=14	0.321969	8.5562	0.42436
N=15	0.362553	7.9512	0.40304
N=16	0.394941	7.5407	0.38314
N=17	0.430838	7.1260	0.35715
N=18	0.474030	6.7025	0.33849
N=19	0.509389	6.4035	0.32328
N=20	0.545176	6.1200	0.30231

Fig 3.12 Effect of etching depth on beam quality (Depth 50 nm)

Depth=60, theta=-14.7	Intensity (a.u.)	fwhm (degree)	Transmission(a.u.)
N=5	0.080022	21.2888	0.65154
N=6	0.100673	18.5824	0.60334
N=7	0.131557	15.8134	0.55134
N=8	0.164154	13.9924	0.51654
N=9	0.191571	12.7734	0.48002
N=10	0.226943	11.4630	0.43878
N=11	0.265592	10.4320	0.41067
N=12	0.296141	9.7740	0.38649
N=13	0.332222	9.0623	0.35406
N=14	0.373945	8.3923	0.32857
N=15	0.406343	7.9564	0.30900
N=16	0.439964	7.5313	0.28392
N=17	0.483889	7.0486	0.26137
N=18	0.520910	6.7013	0.24584
N=19	0.553772	6.4133	0.22683
N=20	0.596778	6.0712	0.20813

Fig 3.13 Effect of etching depth on beam quality (Depth 60 nm)

Depth=70, theta=-14.5	Intensity (a.u.)	fwhm (degree)	Transmission(a.u.)
N=5	0.119442	20.8378	0.45980
N=6	0.144214	18.7265	0.41281
N=7	0.180578	15.9985	0.35391
N=8	0.221980	14.0545	0.30863
N=9	0.251724	12.9312	0.27366
N=10	0.292618	11.5600	0.23487
N=11	0.332750	10.5882	0.20819
N=12	0.361496	9.9813	0.18574
N=13	0.402004	9.1776	0.15909
N=14	0.437598	8.5868	0.14057
N=15	0.464327	8.1787	0.12371
N=16	0.502907	7.6440	0.10615
N=17	0.535453	7.2544	0.09466
N=18	0.561926	6.9530	0.08310
N=19	0.596425	6.5865	0.07156
N=20	0.622686	6.3234	0.06389

Fig 3.14 Effect of etching depth on beam quality (Depth 70 nm)

The simulation results show those two parameters, etching depth and the total number of periods, are very important in the beam quality. We have placed a new sensor in the waveguide after the emission area, and use the first sensor (light red one) as a reference to calculate the transmission, lower transmission means less energy remains in the waveguide and most of the energy is coupled into the air. We also use full width at half maximum here to show the sharpness of the beam pattern. Higher intensity and sharper beam shape means better quality which can be easier detected. With the same etching depth and fill factor, the effective index is almost the same, thus the out-coupling angle is the same (each table has the same angle). Horizontal compare these four tables, it is clear that the out coupling beam angle decreases as the etching depth go deeper.

Chapter IV

Two Beams Steering

4.1 Single Periodicity for Two Beams Coupling

Our work on the effect of periodicity has revealed the possibility of coupling 2 beams out to the air at the same time, e.g. period 950nm. This gave us an idea of using different diffracted orders to realize 2 beams, even multiple beams coupling.

Obviously, more beams being coupled into the air at the same time is a more efficient way to scan the environment for the Lidar application. A larger Field of View (FOV) is also achievable with two beam scanning at the same time. For 1550nm input wavelength, the far-field map of periodicity tuning is shown in Fig 4.1, it shows a very small range of periodicity can match the condition for the second mode coupled out into the air.

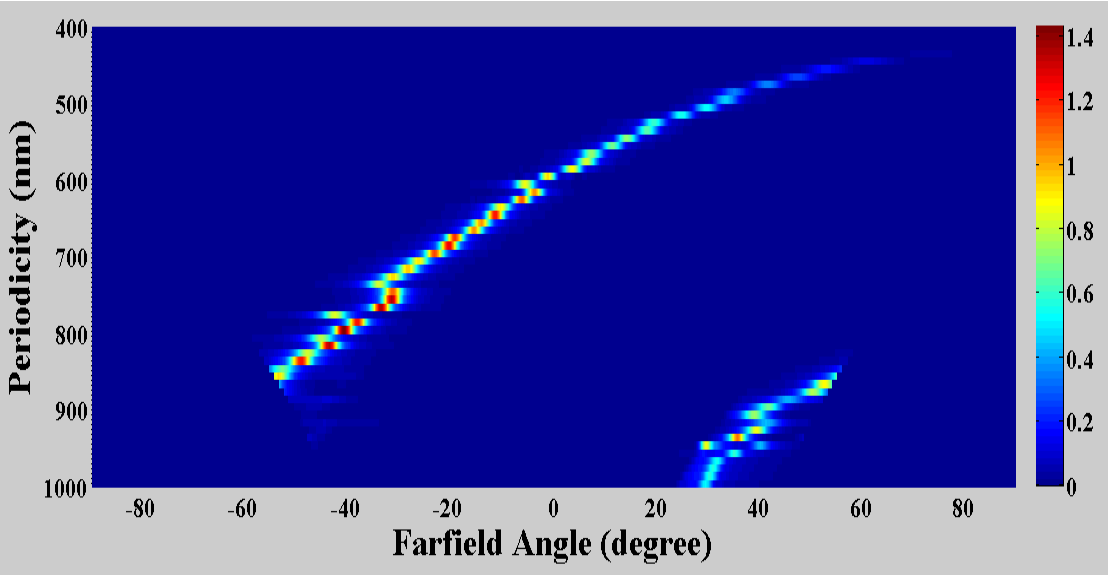

Fig. 4.1 Periodicity (435 nm – 1000nm) tuning map

Let's take an example of 857nm as the periodicity in Fig 4.1. For a periodicity of 857nm, two beams are coupled out into the air at the angle of -55 degree and 55 degree with almost the same intensity. Fig. 4.2 seems a great result for adding the second mode as the tuning angle for scanning.

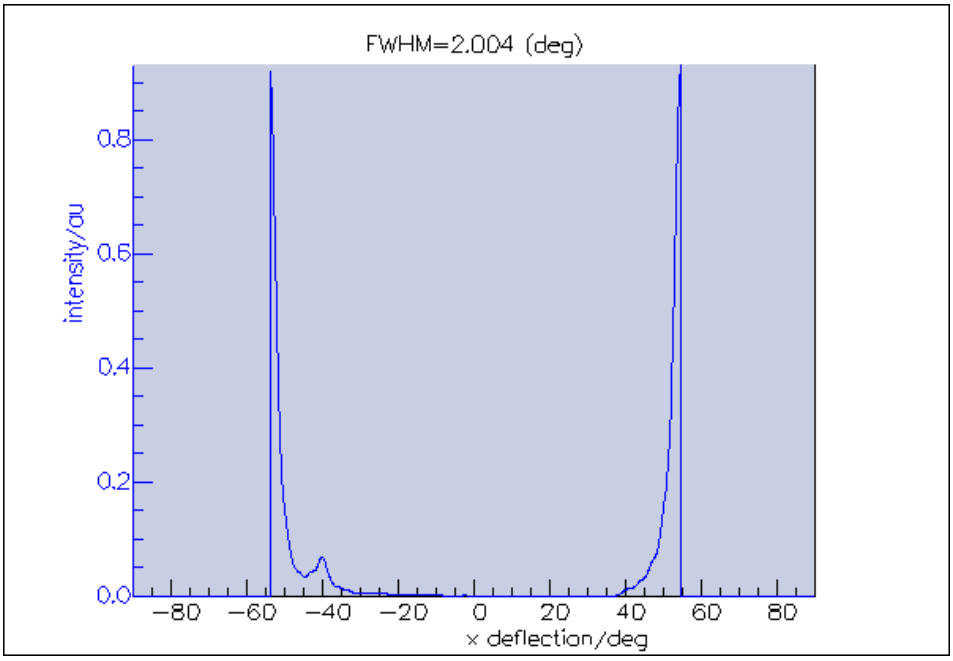

Fig. 4.2 Two beams simultaneously coupled out at the periodicity of 857 nm

However, to continuously tune the out-coupling angle for two diffracted mode is not easy. From the grating equation derived in Chapter 1, the Bragg condition for m=1 and 2 should both be meet at the same time:

$$\sin\theta_m = n_{eff} - m\frac{\lambda_0}{\Lambda} \qquad m = 0, \pm 1, \pm 2, \ldots$$

$$1st\ diffracted\ order\colon\ -1 < n_{eff} - \frac{\lambda_0}{\Lambda} < 1$$

$$2nd\ diffracted\ order\colon\ -1 < n_{eff} - \frac{2\lambda_0}{\Lambda} < 1$$

It clearly shows that, when the effective index is approximately 2.65 (our case), only a periodicity in the range of 849~939 nm is possible for two beams simultaneous coupling. The field of view had no large advantage while utilizing the 1st and 2nd diffracted order at the same time. Another finding is that only the out-coupling angles of 1st and 2nd order are symmetry about the 0 degree, the intensity of two orders are about the same, thus can be detected. Which means, in most cases, the intensity of the 1st diffracted order is always much larger than the other beam. Instead of making the FOV larger, the 2nd order can become a disturbance in the process of detection. It is hard to continuously adjust the out-coupling angle.

4.2 Series Connection of Two Emitting Areas

A new approach for utilizing two beams at the same time is a series connection of two grating area for beam emitting. This seems a very good attempt from the point of engineering. The structure is shown in Fig. 4.3, two grating areas with different periodicity and number of periods are series connected by a waveguide.

To get closer to the application, the input source has a center wavelength of 1550 nm and the tunable range for this laser is 100 nm which is easily found in the market in the area of optical communication.

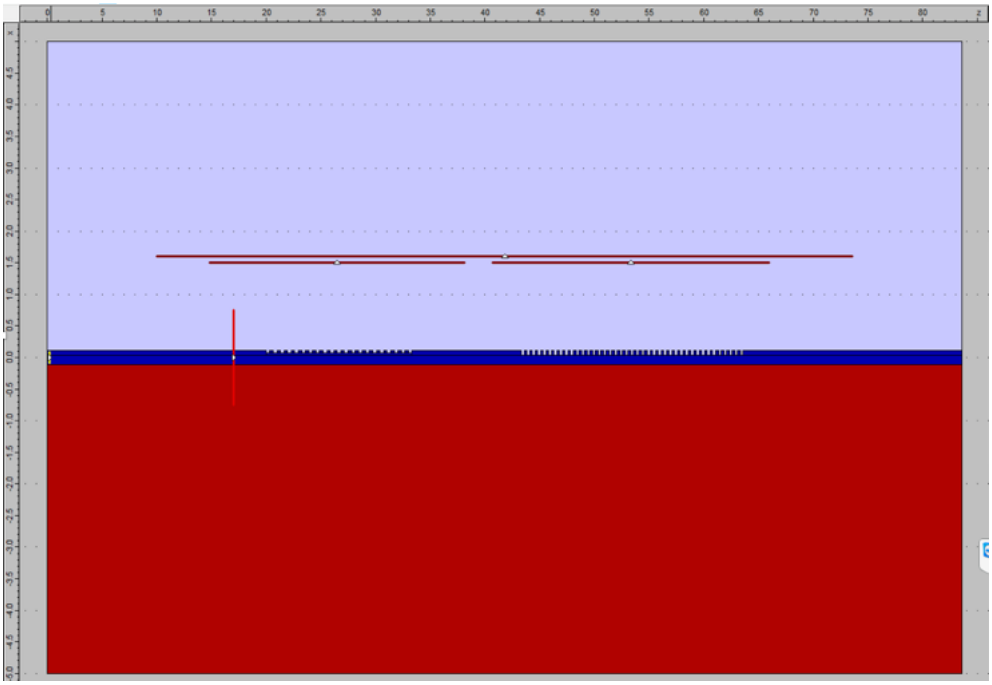

Fig. 4.3 Illustration of series connected design for two beams coupling

There are several technical difficulties for this structure. First, the effective index of refraction will be more complex while there are two different periodic grating on the same waveguide. Ideally, the energy distribution of the two out-coupling beams should be even, this will also need some engineering design. The first grating area is designed to be 650 nm, 40 nm etching depth and only have 20 periods in total, which will couple about 40% of the total energy into the air. For the second grating area, it is optimized as a periodicity of 500 nm with 70 nm etching depth and 50 periods in total. It will couple the remaining energy into

the air to the greatest extent. The simulation results for an input of 1550 nm is shown in Fig. 4.4.

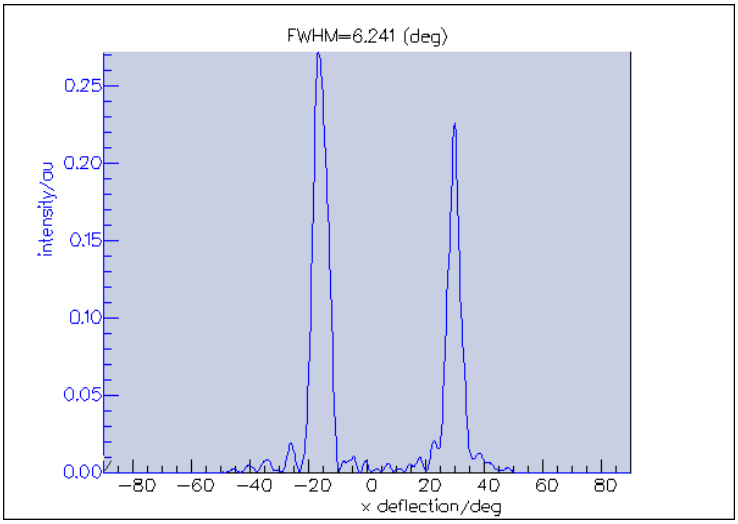

Fig. 4.4 Far-field result of the series connected design at the input of 1550 nm

The two out-coupling angles appear at -16.68 degree and 29.83 degree respectively. The difference between the normalized intensity for the first (0.27) and second beam (0.226) is about 16.9%, which is acceptable for beam detection.

4.3 Compound Grating Coupler for Two Beam Steering

4.3.1 Introduction of the Compound Grating Coupler

We report on a structure designed with a grating coupler with a compound period to generate two out-coupling beams simultaneously. The novel compound period grating coupler can generate two different series of surface harmonic waves at the same time; hence, the energy in the waveguide mode can couple into two different radiation modes. These two radiation modes both satisfy the grating diffraction equation, so they both will respond to wavelength tuning or refractive index tuning. Therefore, within a certain range of wavelength tuning, the two beams both demonstrate a steering range that is comparable to the range of the beam from a traditional single period grating coupler, so the beam steering range of the new compound period grating coupler is approximately doubled compared to a single period grating coupler, and it is not necessary to add extra components such as extra light sources, extra waveguides, or extra chips. Here we propose a new compound period grating coupler

formed by combining two grating structures with different periodicities. The new compound period grating coupler structure can couple the waveguide mode into two radiation modes with different angles. Therefore, the beam steering range is doubled due to the extra beam. We numerically demonstrate this method using 2-D FDTD simulation, and a $\mathbf{26.20}^{\circ}$ steering range is observed within a wavelength tuning range of 1500 nm to 1600 nm.

4.3.2 Coupling Mechanism

For the compound grating structure, it is hard to understand the coupling mechanism by the normal geometrical theory. Let's go back to the basic model of the grating coupler with a single periodicity. In most studies concentrating on Si-based grating couplers, the device is fabricated on an SOI (silicon on insulator) wafer [1-2, 8]. Fig. 4.5 shows the side cross-section of a typical SOI based grating coupler, it contains a 220 nm-thick Si waveguide on top of an oxide layer with a thickness of 2 μm. The Si layer of 220 nm is etched first to form the waveguide layout; secondly, waveguides are etched for 70 nm to form the grating structure on the waveguides.

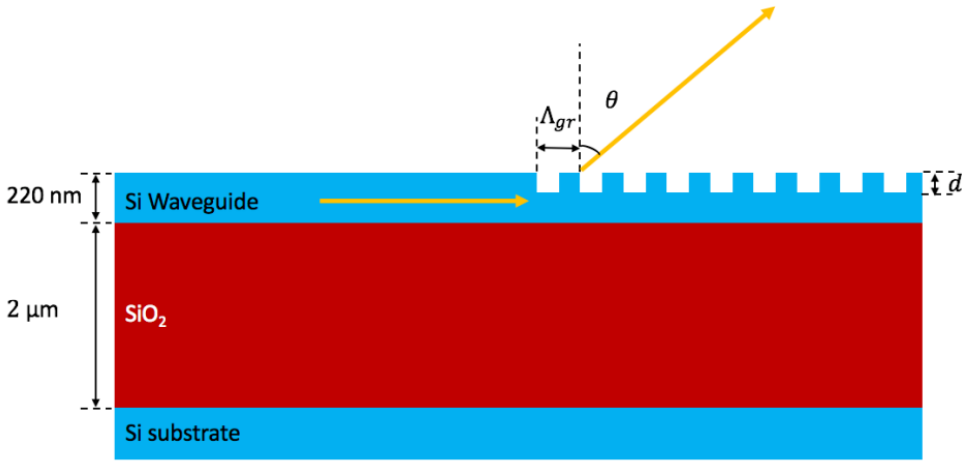

Fig. 4.5 Illustration of single period grating coupler. Λ is the periodicity, d is the grating depth, and θ is the out-coupling angle.

The out-coupling angle of this grating coupler structure is governed by the grating equation, which is shown as:

$$\sin\theta_m = n_{eff} - m\frac{\lambda_0}{\Lambda} \qquad m = 0, \pm 1, \pm 2, \ldots$$

where Λ is the periodicity of the gratings; θ_m is the out-coupling angle; and m is an integer, the diffraction order. This equation describes the phase match condition between the waveguide mode and the radiation mode, which we have already explained a lot in the previous chapters.

$$E(\vec{r}) = A(\vec{r})e^{-j\overrightarrow{k_{inc}}\cdot\vec{r}}$$

$$= A\left[\varepsilon_{r,avg} + \Delta\varepsilon\cos(\vec{K}\cdot\vec{r})\right]e^{-j\overrightarrow{k_{inc}}\cdot\vec{r}}$$

$$= A\,\varepsilon_{r,avg}e^{-j\overrightarrow{k_{inc}}\cdot\vec{r}} + \frac{A\Delta\varepsilon}{2}e^{-j(\overrightarrow{k_{inc}}-\vec{K})\cdot\vec{r}} + \frac{A\Delta\varepsilon}{2}e^{-j(\overrightarrow{k_{inc}}+\vec{K})\cdot\vec{r}}$$

Now, a single wave has been split into three waves due to the grating, one in the original direction and two directions on either side of the central direction. Each of those waves can be split into three waves as well, and then goes on to infinity.

$$e^{-j\overrightarrow{k_{inc}}\cdot\vec{r}} \rightarrow \begin{cases} e^{-j\overrightarrow{k_{inc}}\cdot\vec{r}} \\ e^{-j(\overrightarrow{k_{inc}}-\vec{K})\cdot\vec{r}} \\ e^{-j(\overrightarrow{k_{inc}}+\vec{K})\cdot\vec{r}} \end{cases} \qquad e^{-j(\overrightarrow{k_{inc}}-\vec{K})\cdot\vec{r}} \rightarrow \begin{cases} e^{-j(\overrightarrow{k_{inc}}-\vec{K})\cdot\vec{r}} \\ e^{-j(\overrightarrow{k_{inc}}-2\vec{K})\cdot\vec{r}} \\ e^{-j\overrightarrow{k_{inc}}\cdot\vec{r}} \end{cases} \qquad e^{-j(\overrightarrow{k_{inc}}+\vec{K})\cdot\vec{r}} \rightarrow$$

$$\begin{cases} e^{-j(\overrightarrow{k_{inc}}+\vec{K})\cdot\vec{r}} \\ e^{-j\overrightarrow{k_{inc}}\cdot\vec{r}} \\ e^{-j(\overrightarrow{k_{inc}}+2\vec{K})\cdot\vec{r}} \end{cases} \quad \dots$$

The grating structure makes this possible as it generates a series of surface harmonic waves due to the periodical spatial fluctuation of the refractive index. In the grating area, the electrical field distribution of the waveguide mode can be expressed as the sum of all the possible harmonic waves [25], that is:

$$\boldsymbol{E}_{grating} = \sum_{m=-\infty}^{\infty} A_m \cdot e^{-j(\overrightarrow{k_{inc}}-m\vec{K})\cdot\vec{r}}$$

where A_m is the amplitude of the m^{th} order harmonic wave, $\boldsymbol{k}_{inc}$ is the wave vector of the incident wave, in a typical grating coupler, we use **K** as the grating vector, the magnitude of the grating vector $|\boldsymbol{K}| = \frac{2\pi}{\Lambda}$.

one of these altered propagation constants exactly matches the wavenumber of a specific radiation mode, and the other propagation constants don't satisfy this phase match. Therefore, the energy in the waveguide mode is able to couple to this radiation mode, and the coupling

efficiency tends to approach unity when the number of gratings increases. The reason that only one propagation constant satisfies the phase match condition is that the term sinθ in Equation 1 has to be in the range of (-1,1).

In principle, if a structure can generate different series of the surface harmonic waves with different periodicity, then the electrical field in the structure can be expressed as:

$$E_{grating} = \sum_{m_1=-\infty}^{\infty} A_{m_1} \cdot e^{-j(\overrightarrow{k_{inc}} - m_1\overrightarrow{K_1})\cdot\vec{r}} + \sum_{m_2=-\infty}^{\infty} A_{m_2} \cdot e^{-j(\overrightarrow{k_{inc}} - m_2\vec{K}_1)\cdot\vec{r}} + \cdots + \sum_{m_n=-\infty}^{\infty} A_{m_n} \cdot e^{-j(\overrightarrow{k_{inc}} - m_n\overrightarrow{K_n})\cdot\vec{r}}$$

In this case, there is a possibility that more than one harmonic wave can satisfy the phase match condition. Therefore, multiple out-coupling beams will be emitted from the structure.

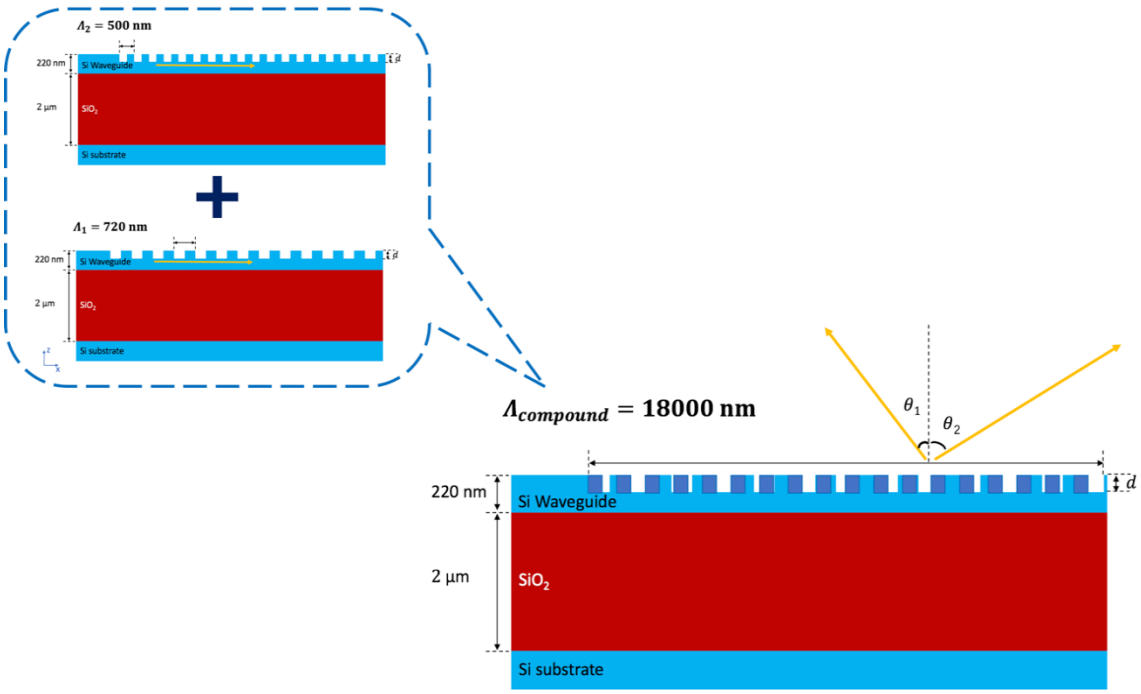

Fig. 4.6 Illustration of the compound period grating coupler structure.

In this work, we design a grating structure in which the configuration of the grating is the combination of two gratings with different periodicities. Fig. 4.6 shows the side cross-section of the structure. We combined 36 gratings with the periodicity of 500 nm and 25 gratings with the periodicity of 720 nm to form a new grating structure with an envelope periodicity of 18000 nm; here we name the two gratings with single periodicity the component gratings and the new structure the compound period grating. To ensure

consistency with previous studies, the grating's thickness is 70 nm; the thickness of the waveguide layer is 220 nm; a 2 μm SiO2 substrate layer is placed below the waveguide layer, and only one envelope period of the compound period grating is considered in this work. The fill factor of the two component gratings is 0.5 and the new compound period grating has a fill factor of 0.64. The refractive index of Si and SiO2 are set to be 3.477 and 1.450 respectively at a vacuum wavelength of 1550 nm. In this work, the 2-D FDTD (finite difference time domain, OmniSim) is utilized. A sinusoidal pulse with TE polarization is applied to the Si waveguide for the simulation.

Because of the combining of the two periodical spatial fluctuations of the refractive index with different periodicities, the electrical field distribution of the waveguide mode becomes the sum of two series of harmonic waves:

$$E_{grating} = \sum_{m_1=-\infty}^{\infty} A_{m_1} \cdot e^{-j[k_{inc}+m_1(2\pi/\Lambda_1)]} + \sum_{m_2=-\infty}^{\infty} A_{m_2} \cdot e^{-j[k_{inc}+m_2(2\pi/\Lambda_2)]}$$

where $\Lambda_1 = 720$ nm and $\Lambda_2 = 500$ nm.

Hence, the phase match condition is satisfied between the waveguide mode and the two radiation modes at the same time. The first radiation mode forms a beam with an out-coupling angle θ_1 that satisfies:

$$sin\theta_1 = n_{eff} + m_1 \cdot (\frac{\lambda_0}{\Lambda_1})$$

And the second radiation mode satisfies:

$$sin\theta_2 = n_{eff} + m_2 \cdot (\frac{\lambda_0}{\Lambda_2})$$

4.3.3 Simulation Result Analysis

Fig. 4.7 shows the far field angle distribution of the compound period grating coupler at a wavelength of 1550 nm, calculated using the far field calculator in the OmniSim software, the direction of the angle is parallel to the waveguide. The intensity in the far-field figure is automatically normalized and knowing how much energy is distributed in this far field pattern, we can estimate the intensity of each beam. The ratio of the energy coupled to the air relative to the input energy for this wavelength is 31.60%; this ratio of the input energy is

distributed in these two beams. The positive value in the far field angle is the θ1 in Figure 4.7, and the negative value is the opposite, as θ_2.

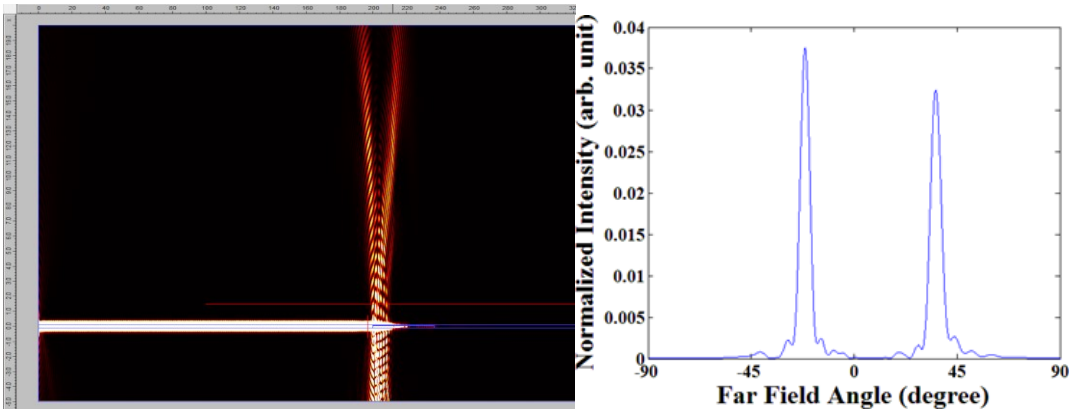

(a) **(b)**

Fig. 4.7 Far-field simulation result of the compound period grating coupler with an applied wavelength of 1550 nm. (a) Field distribution (b) Normalized intensity

As shown in Figure 4.7, when the input is at 1550 nm, two beams are generated by the compound period grating structure; the first has a far-field angle of 35.67°, normalized intensity of 0.0324, and a FWHM (full width at half maximum) of 5.48°, while the second has a far-field angle of -21.38°, normalized intensity of 0.0375, and a FWHM of 4.86°. The first beam is generated by the harmonic wave with the periodicity of 720 nm, and the second is generated by the harmonic wave with the periodicity of 500 nm, noted as Beam 1 and Beam 2 respectively. Beam 2 contains a slightly higher intensity and narrower FWHM, showing a better quality than Beam 1. This is because the 500 nm period grating has 11 more gratings than the 720 nm period grating. The SiO2 substrate has a higher refractive index than the air, so 56.86% of the input energy is coupled to the substrate, which is more than the energy coupled to the air (31.60%). Besides the energy coupled to the radiation modes, 4.86% of the light is transmitted; it keeps propagating inside the waveguide because the grating number of the structure is not large enough to couple out all the energy from the waveguide mode. 7.15% of the input energy is reflected, finally going in the opposite direction to the waveguide; this is because the spatial fluctuation created by the grating structure also forms a weak DBR (distributed Bragg reflector) structure, which results in the reflection.

To achieve solid-state beam steering, we utilize wavelength tuning in this work. Fig. 4.8

(a) shows the far-field angle contour map of the compound period grating structure versus the wavelength; we tested the wavelengths from 1300 nm to 1800 nm with intervals of 10 nm.

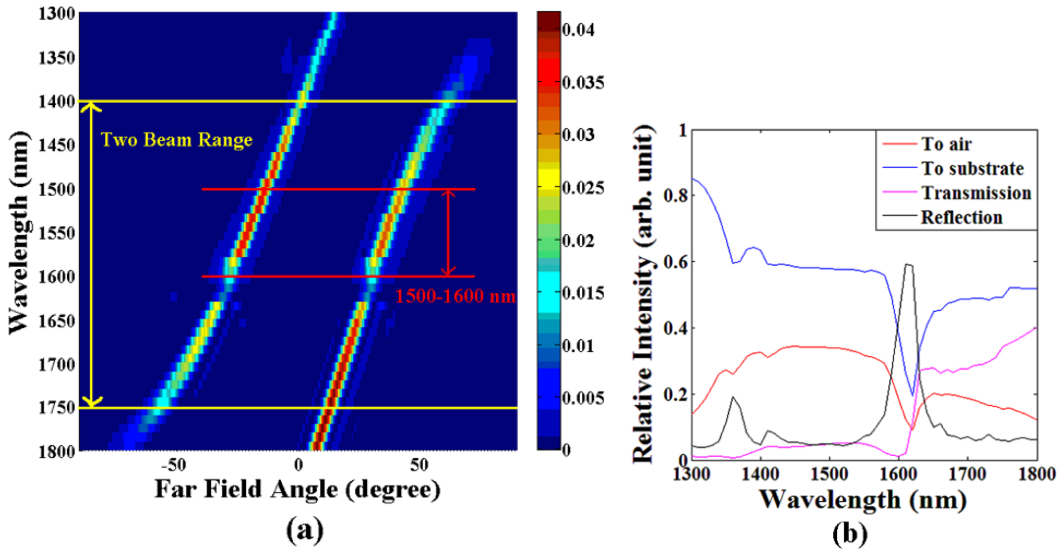

Fig. 4.8 Performance of compound period grating coupler V.S. Applied wavelength. (a) Far-field contour map; (b) Energy flow.

To be consistent with the previous studies, the beam steering range within the wavelength of 1500 nm to 1600 nm is analyzed. As shown in Figure 4.8 (a), the red line indicates the beam steering range of the two beams at this wavelength range. Beam 1 varies from 42.59° at 1500 nm to 30.53° at 1600 nm and a beam steering range of 12.06° is achieved with only slight variation of FWHM (e.g. 5.73° at 1500 nm and5.79°, and a maximum value of 6.16° at 1590 nm). Beam 2 varies from -13.94° at 1500 nm to -28.08° at 1600 nm and the beam steering range is 14.14°. The FWHM of Beam 2 also varies by a neglectable value: it is 4.50° at 1500 nm and 5.85° at 1600 nm; the maximum value is 6.10° at 1590 nm and the minimum value is 4.50° at 1500 nm. In summary, the total beam steering range is calculated by adding the two beam steering ranges is 26.20°. As a comparison, the previous study with a single period grating structure achieved a beam steering range of 14.10° in the same wavelength tuning range [1]. Hence, with the compound period grating structure, the total beam steering range is approximately doubled.

The yellow line in Fig. 4.8 (a) indicates the total range of variation of the compound period grating structure. This range is selected because the intensity of both beams is

sufficiently high. The total range contains the wavelengths of 1400 nm to 1750 nm. In this range, the far-field angle of Beam 1 varies from 60.94° to 12.48°. When the applied wavelength is smaller than 1400 nm, Beam 1 gradually vanishes because Equation 4 is no longer satisfied. The FWHM of Beam 1 has a maximum value of 7.90° at 1400 nm in the two-beams range; this large FWHM is formed because when the out-coupling beam has a larger angle, it becomes harder for the grating structure to converge the energy. The minimum value of FWHM of Beam 1 is 4.53° at 1630 nm, so it can be concluded that the Beam 1 is converged in the total two beam range. The far field angle of Beam 2 varies from 1.18° at 1400 nm to -58.02° at 1750 nm, and the whole steering range is 59.20°, which is 10.74° higher than Beam 1. This is because Beam 2 is created by the surface harmonic wave with the periodicity of 500 nm, while the surface harmonic wave for Beam 1 has a periodicity of 720 nm. Therefore, the sensitivity of the far field angle to the wavelength of Beam 2 is higher than Beam 1. The FWHM of Beam 2 has a maximum value of 8.67° at 1750 nm and a minimum value of 4.07° at 1410 nm, so Beam 2 is also converged in this range.

In summary, from 1400 nm to 1750 nm, Beam 1 covers the angle from 60.94° to 12.48° and Beam 2 covers from 1.18° to -58.02°; a total steering range of 107.66° is achieved with a wavelength tuning range of 350 nm (1400 nm to 1750 nm). In addition, the center angle range from 1.18° to 12.48° can also be covered in two approaches: one is to utilize Beam 1 at wavelengths higher than 1750 nm and the other is to utilize Beam 2 at wavelengths lower than 1400 nm.

The normalized intensity of the two beams is shown by the color map in Fig. 4.8 (a) which is calculated by the far field calculator in the FDTD software. Fig. 4.8 (b) shows the energy flow of the whole system where the red line is the energy coupled to the air and shows how much energy is distributed in the two beams due to the wavelength; the blue line is the energy coupled to the SiO2 substrate, which is higher than the energy to the air in the whole range; the purple line shows the transmission; and the black line shows the reflection.

In Fig. 4.8 (a), both of the two beams are weak at the wavelength around 1610 nm and Fig. 4.8 (b) shows that a notable reflection peak appears at this wavelength where 59.29%

and 58.61% of the energy is reflected at 1610 nm and 1620 nm, respectively. This may be because the two surface harmonic waves with a periodicity of 720 nm and 500 nm both form a weak DBR structure and their response wavelength overlap at this wavelength, thus resulting in an especially high reflection peak at the wavelength around 1610 to 1620 nm. On the other hand, the lowest value of the energy coupled to the air is 9.00% at the wavelength of 1620 nm, while the highest energy to the air in the two-beams range is 34.30% at the wavelength of 1470 nm; thus, the lowest energy coupled to the air is 26.24% of the highest. Considering that the energy is shared approximately evenly by the two beams at the wavelength of 1620 nm, we estimate that the intensity of the two beams at this wavelength are still adequate to be detected. It also can be observed in Fig. 4.8 that when the applied wavelength is close to 1300 nm or 1800 nm, one of the two beams gradually vanishes, also resulting in a reduction of the energy coupled to the air. When the energy to the air drops, the reduced part of the energy either couples to the substrate or stays in the waveguide mode. In summary, the compound period grating coupler shows a good performance in the whole two-beams range with an exception at 1610-1620 nm. Due to the high reflection peak, the intensity of the out-coupling beams shows a minimum value at 1620 nm, which is approximately one fourths of the maximum intensity at 1470 nm. In the real case, this issue may be a problem to some of the applications such as solid-state Lidar, which requires a high beam intensity to achieve a long detection range. So, in these kinds of applications, researches may want to avoid to utilizing the wavelength tuning at this wavelength range. While the fact that the minimum intensity is still about one fourths of the highest also shows the possibility that this wavelength range is still applicable in some case when the requirement of beam intensity is not extremely tight.

By using this compound period grating coupler, the energy coupled to the air is shared by two beams, so, if we assume the light source is constant, this fact means the increased beam steering range is achieved with a cost of decreased beam intensity. This gives us a chance to balance the tradeoff between the beam steering range and the beam intensity.

When this compound period grating structure is applied to some of the applications such as solid-state Lidar, an on-chip solution to distinguish the reflection signal from the two

beams at the detection end will be necessary. In a previous study, an on-chip photodetector that can detect the direction of the incident light is reported [26]. In this work, a metal wall is integrated on the chip that separates two adjacent photodiodes in the same area. When the incident signal has an angle to the normal direction, one of the photodiodes will be illuminated the whole area, while the other is only illuminated a part of the area because of the metal wall forming a shadow, so by carefully comparing the different response from the two photodiodes, the incident angle of the signal can be distinguished. In principle, this work can be applied to our work to distinguish the two beams generated simultaneously. Of course, this is only one of the data processing solutions for the practical Lidar application.

4.4 Optimization and Fabrication Tolerance

In this work, the two component gratings are combined to form a compound period grating structure. However, the compound period grating structure contains several gaps whose widths are extremely small. The smallest gap has a width of 10 nm, and considering that the depth of the grating is 70 nm, the aspect ratio of this gap is 7; this high aspect ratio is hard to fabricate using CMOS processing technology [28]. On the other hand, the coupling between the waveguide mode and the radiation mode is achieved by the surface harmonic wave, therefore, the disappearance of some of the gratings in a large number of gratings will weaken the surface harmonic wave but not eliminate it. Thus, we can predict that if some of the narrow gaps cannot be fabricated, the whole performance of the device will not change too substantially. Figure 4.9 illustrates what the structure is like if some of the gaps cannot be fabricated.

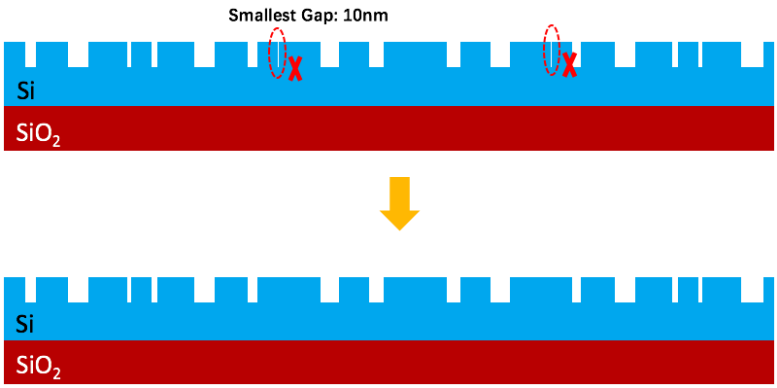

Fig. 4.9 Illustration of the structure without the gaps cannot be fabricated.

Fig. 4.10 shows the far-field contour map and the energy flow diagram when some of the gaps are not able to be fabricated. The traditional SiO2 substrate structure is considered in this result. Here we test all the gaps with a width under 100 nm, because a gap with 100 nm width and 70 nm depth promises to be easily fabricated with current COMS processing techniques.

In Fig. 4.10 (a), it can be observed that the far field angle of Beam 1 is 35.67° when all the gaps can be fabricated, and that it varies to 36.57° when all the gaps under 100 nm cannot be fabricated. A slight increase of the far field angle occurs because the total effective refractive index is also increased when the air gaps are replaced by Si. The FWHM of Beam 1 has almost no variation. Beam 2 has the same trend as Beam 1: the far field angle in Fig. 4.10 (a) varies from -21.38° to -20.42°.

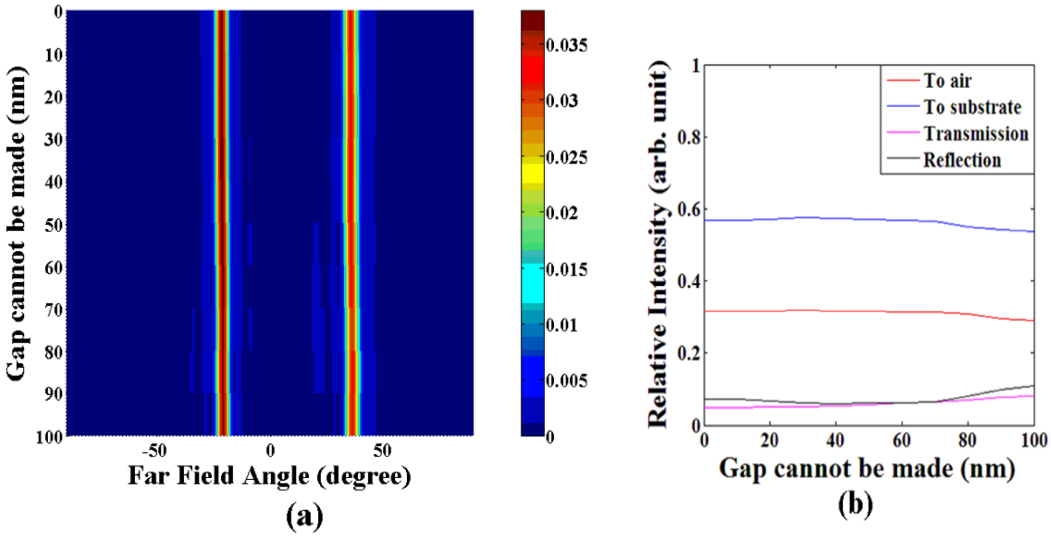

Fig. 4.10 Performance of compound period grating coupler considering the fabrication tolerance of high aspect ratio gaps. (a) Far-field contour map; (b) Energy flow.

Figure 4.10 (b) shows the energy flow diagram of the result. It can be observed that all the lines are approximately flat; the energy to the air varies from 31.60% to 28.97%, making the difference negligible. Therefore, it can be concluded that the compound period grating structure has a non-demanding fabrication tolerance and will not have its potential limited by the current CMOS processing technology.

4.5 Conclusion for Compound Period Grating

In this work, we propose and numerically demonstrate the compound period grating structure. With this structure, the traditional grating coupler can be modified to generate two out-coupling beams simultaneously and because of the extra beam, the beam steering range of the device is doubled. A total beam steering range of 26.20° is achieved within a wavelength tuning range of 100 nm (1500 nm to 1600 nm), and a total beam steering range of 107.66° is achieved within a wavelength tuning range of 350 nm. In addition, this result can potentially be improved through optimization and by combining with other studies, such as that using the photonic crystal as the waveguide [7].

The fabrication tolerance of the compound period grating structure is studied in consideration of cost efficiency and the result shows that the structure retains good performance even if all the gaps under 100 nm cannot be fabricated. Thus, we can claim that the compound period grating structure has great potential for many applications such as telecommunication and sensing, especially for solid-state Lidar technology.

When this compound period grating structure is applied to the solid-state Lidar technique, both of the reflections of the two out-coupling beams will be detected, making it necessary to have a method to distinguish between the two beams at the detection end. In a previous study, an on-chip photodetector that can detect the direction of the incident light was reported [25]. A metal wall is integrated on the chip to separate two adjacent photodiodes with the same area; when the light incidents from a not-normal direction, one of the photodiodes will be illuminated over the whole area, while the other is illuminated over only a part of the area because the metal shadows a part of the light. This study can be applied to distinguish the two beams of the compound period grating structure at the detection end. The Lidar technique detects the time interval between the ejected light and its reflection, allowing for the calculation of the distance of the reflector. When the compound period grating structure is applied, two out-coupling beams will be ejected at the same time and we will then have two cases at the detection end. First, the detection end detects two reflection signals, and in this case the on-chip direction-sensitive photodetector will give us the information about

which beam is coming from which direction; second, if the detection end detects only one reflection signal, then we can estimate that the two beams also reflect at the same time, so the two reflectors are at the same distance.

Chapter V

Measurement of Linear Polarization Distinguishing Metalens

5.1 Introduction Polarization Distinguishing Metalens

In this study, for the first time, a metalens is designed with the ability to distinguish linear polarization while maintaining concentrating performance comparable with the state-of-the-art metalens under linear polarized incidence. This design is achieved through the novel design of anisotropic phase shifter with scattering effect on unwanted polarization while maintaining continuous phase shift on the orthogonal polarization.

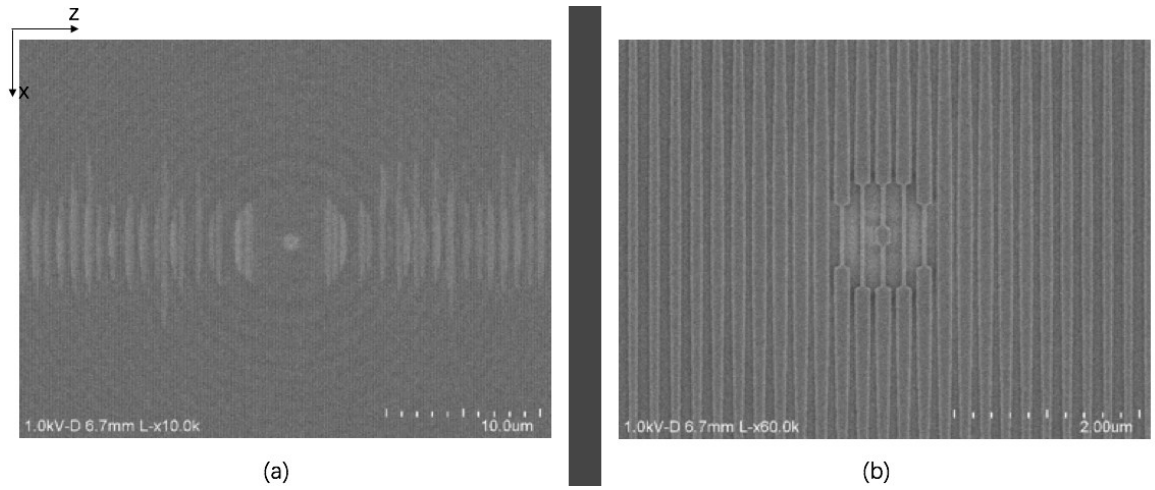

Fig. 5.1 SEM image of the lens (a) Overall View of the Metalens; (b) Zoomed in Center Area (5×5 μm).

A polarization distinguishing lens with diameter of 40 μm and numerical aperture of 0.9 (NA=0.9) for input wavelength of 685 nm is first simulated with the FDTD simulation tool by Mao Ye, PhD student in Integrated Nano Photonics and Electronics Laboratory at University of Michigan, and then fabricated with CMOS compatible nanofabrication techniques in Lurie Nanofabrication Facility. This is the first focusing metalens designed with linear polarization distinguishing effect. In order to achieve linear polarization distinguishing effect, Mao has designed a novel phase shifter that is highly sensitive to the variation of linear polarization. The lens material for designing this novel metalens is silicon rich silicon nitride (SiNx) with the refractive index of 2.74, extinction coefficient k = 0 at the design

wavelength of 685 nm. This material is also an innovation, specially designed for metalens.

The SEM picture of the sample is taken after gold sputtering. The overall view is shown in Fig. 5.1 (a), Fig. 5.1 (b) shows a zoom-in view of the 5×5 μm area at the center of lens. The structure is physically formed by individual lines with width varied on x-direction. The smallest feature is around 48 nm as measured.

5.2 Measurement of Linear Polarization Distinguishing Metalens

The optical characterization system for the Linear Polarization Distinguishing Metalens is shown in Fig. 5.2.

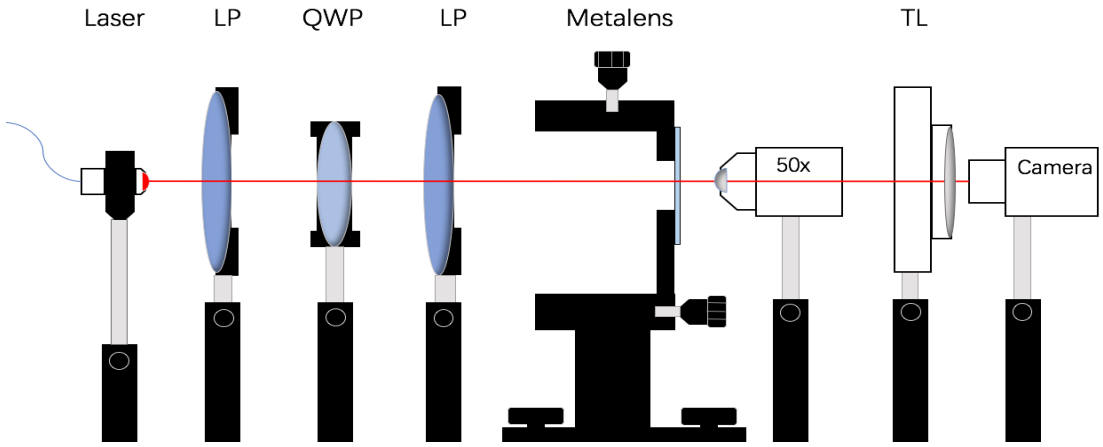

Fig. 5.2 Illustration of the optical characterization system

A diode laser of 685 nm (LP685-SF15, Thorlabs) is applied as the light source. Although the laser is linearly polarized, we still applied a linear polarizer (LP) after the light source to achieve a better polarization. Secondly, a quarter wave plate (QWP) is applied to turn the light into circularly polarization. After the quarter wave plate, the second linear polarizer is fixed on a rotation mount to achieve linear polarized light with tunable direction. The diameter of the laser spot passes the metalens sample is larger than 1 cm which can be considered as plane wave when the center is collimated to our lens (the size of the lens is 40 μm). The image acquired is magnified by an Olympus 50X objective lens and finally received by a camera (DCC3240C, Thorlabs) through a tube lens (TL). The sample is loaded on a 3-D axis motion system (MT3A, Thorlabs) with smallest movement of 500 nm.

The measured field distribution on the plane of focus is shown in Fig. 5.3(a) for the incidence of Ez (at 175° of LP 2) and Fig. 5.3(b) for the incidence of Hz (at 265° of LP2).

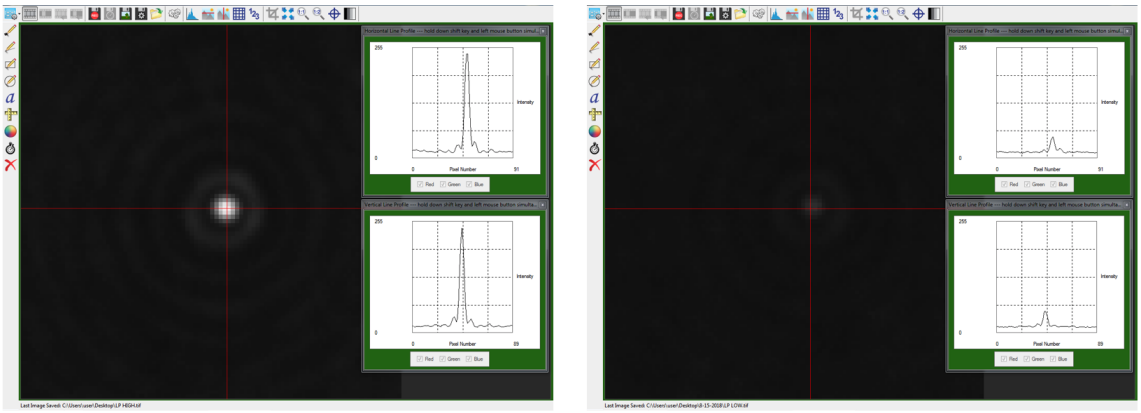

(a) (b)

Fig. 5.3 Measurement results for Linear Distinguishing Metalens (a) Ez Direction (b) Hz Direction

It can be observed that a clear focus is formed under the incidence of designed linear polarization Ez in Fig. 5.3(a) for round 53 times of the incident intensity with full-width-at-half-maximum (FWHM) of 0.9 μm, and there is hardly any focusing when the incident polarization is tuned by 90 degrees in Fig. 5.3(b) while the background of measurement didn't change much. The peak intensity at designed polarization Ez is around 8 times of intensity at polarization Hz.

Chapter VI

Conclusion

This thesis introduced the three main research projects completed by the author including one beam grating coupler, compound grating coupler for two beams steering and the measurement of Linear Distinguishing Metalens. The mechanism of one beam free-space coupling is introduced, the effects of different parameters in the grating coupler design, such as period size, number of total periods and etching depth are simulated and analyzed by FDTD method. And base on the numerical study of one beam grating coupler, we have proposed a novel design of a compound period grating coupler formed by mathematically combining two grating structures with different periodicities. The new compound period grating coupler structure can couple the waveguide mode into two radiation modes with different angles. Therefore, the beam steering range is doubled due to the extra beam. We numerically studied this idea, and a $26.20°$ steering range is observed within a wavelength tuning range of 1500 nm to 1600 nm. In addition, the investigation of fabrication tolerance shows that the new structure can be fabricated with the current CMOS technology.

REFERENCES

[1] K. V. Acoleyen, W. Bogaerts, J. Jagerska, N. L. Thomas, R. Houdre, and R. Baets. "Off-chip beam steering with a one-dimensional optical phased array on silicon-on-insulator". *Optics Letters*, 34(9), pp. 1477–1479 (2009).

[2] K. V. Acoleyen, W. Bogaerts, and R. Baets. "Two-dimensional dispersive off-chip beam scanner fabricated on silicon-on-insulator". *IEEE Photonics Technology Letters*, 23(17), pp. 1270–1272 (2011).

[3] J. K. Doylend, M. J. R. Heck, J. T. Bovington, J. D. Peters, L. A. Coldren, and J. E. Bowers. "Two-dimensional free-space beam steering with an optical phased array on silicon-on-insulator". *Optics Express*, 19(22), pp. 21595–21604 (2011).

[4] J. K. Doylend, M. J. R. Heck, J. T. Bovington, J. D. Peters, M. L. Davenport, L. A. Coldren, and J. E. Bowers. "Hybrid III/V silicon photonic source with integrated 1D free-space beam steering". *Optics Express*, 37(20), pp. 4257–4259.

[5] W. Guo, P. R. Binetti, C. Althouse, M. L. Masanovic, H. P. Ambrosius, L. A. Johansson, and L. A. Coldre. "Two-dimensional optical beam steering with InP-based photonic integrated circuits". *IEEE Journal of Selected Topics in Quantum Electronics*, 19(4), pp. 6100212–6100212 (2013).

[6] J. C. Hulme, J. K. Doylend, M. J. R. Heck, J. D. Peters, M. L. Davennport, J. T. Bovington, L. A. Coldren, and J. E. Bowers. "Fully integrated hybrid silicon two-dimensional beam scanner". *Optics Express*, 23(5), pp. 5861–5874 (2015).

[7] K. Kondo, T. Tatebe, S. Hachuda, H. Abe, F. Koyama, and T. Baba. "Fan-beam steering device using a photonic crystal slow-light waveguide with surface diffraction grating". *Optics Letters*, 42(23), pp. 4990–4993 (2017).

[8] S. K. Selvaraja, P. Jaenen, W. Bogaerts, D. V. Thourhout, P. Dumon, and R. Baets. "Fabrication of photonic wire and crystal circuits in silicon-on-insulator using 193-nm optical lithography". *IEEE Journal of Lightwave Technology*, 27(18), pp. 4076–4083 (2009).

[9] L. Zhu, W. Yang, C. Chang-Hasnain. "Very high efficiency optical coupler for silicon nanophotonic waveguide and single mode optical fiber". *Optics Express*, 25(15), pp. 18462–18473 (2017).

[10] E. Garmire, J. M. Hammer, H. Kogelnik, and F. Zernike. Integrated Optics., 1979.

[11] K. Yee. "Numerical solution of initial boundary value problems involving Maxwell's equations in isotropic media". *IEEE Transactions on Antennas and Propagation*, 14 (3): 302–307 (1996).

[12] A. Taflove, S. C. Hagness. Computational Electrodynamics: The Finite-Difference Time-Domain Method, 3rd ed. Artech House Publishers (2005). ISBN 1-58053-832-0.

[13] I. Valuev, A. Deinega; S. Belousov. "Iterative technique for analysis of periodic structures at oblique incidence in the finite-difference time-domain method." *Optics Letters*, 33: 1491 (2008).

[14] A. Aminian, Y. Rahmat-Samii. "Spectral FDTD: a novel technique for the analysis of oblique incident plane wave on periodic structures." *IEEE Transactions on Antennas and Propagation*, 54: 1818–1825 (2006).

[15] A. Deinega, S. Belousov; I. Valuev. "Hybrid transfer-matrix FDTD method for layered periodic structures." *Optics Letters*, 34: 860-862 (2009).

[16] Y. Hao, R. Mittra. FDTD Modeling of Metamaterials: Theory and Applications. Artech House Publishers (2009).

[17] J. Berenger. "A perfectly matched layer for the absorption of electromagnetic waves". *Journal of Computational Physics*, 114 (2): 185–200 (1994).

[18] S. D. Gedney. "An anisotropic perfectly matched layer absorbing media for the truncation of FDTD lattices". *IEEE Transactions on Antennas and Propagation*, 44 (12): 1630–1639 (1996).

[19] J. W. Goodman. Introduction to Fourier Optics. McGraw-Hill, Inc., 1986.

[20] D. Taillaert. Grating Couplers as Interface Between Optical Fibers and Nanophotonic Waveguides. UGent, PhD Thesis, 2006.

[21] G. Roelkens, D. V. Thourhout, and R. Baets. "High efficiency grating coupler between silicon-on-insulator waveguides and perfectly vertical optical fibers". *Optics Letters*, 32(11):1495–1497 (2007).

[22] G. Roelkens, D. Vermeulen, D. V. Thourhout, R. Baets, S. Brision, P. Lyan, P. Gautier, J. M. Fedeli. "High efficiency diffractive grating couplers for interfacing a single mode optical fiber with a nanophotonic silicon-on-insulator waveguide circuit". *Applied Physics Letters*, 92(13):131101 (2008).

[23] S. Scheerlinck. Metal grating and polymer based coupling components for photonic integrated circuits. UGent, PhD Thesis, 2008.

[24] K. V. Acoleyen. Nanophotonics beamsteering elements using silicon technology for wireless optical applications. UGent, PhD Thesis, 2011.

[25] T. Tamir and S. T. Peng. "Analysis and design of grating coupler". *Applied Physics A: Materials Science& Processing*, 14(3), pp. 235–254 (1977).

[26] H. Wang, T. Luo, H. Song, and J. B. Christen. "On-chip sensor for light direction detection". *Optics Letters*, 38(22), pp. 4554–4557 (2013).

[27] F. Vasey, F. K. Reinhart, R. Houdré, and J. M. Stauffer. "Spatial Optical Beam Steering with an Algaas Integrated Phased-Array". *Applied Optics*, 32(18):3220–3232 (1993).

[28] W. Bogaerts, S. Selvaraja, P. Dumon, J. Brouckaert, K. De Vos, D. Van Thourhout, and R. Baets. "Silicon-on-Insulator Spectral Filters Fabricated with CMOS Technology". *Journal of Selected Topics in Quantum Electronics*, 16(1):33–44 (2010).

[29] N. Eriksson, M. Hagberg, and A. Larsson, "Highly directional grating outcouplers with tailorable radiation characteristics". *IEEE Journal of. Quantum Electronics*, vol. 32, pp. 1038-1047, (1996).

[30] O. Beyer, I. Nee, F. Havermeyer, and K. Buse, "Holographic recording of Bragg gratings for wavelength division multiplexing in doped and partially polymerized poly (methyl methacrylate)". *Applied Optics*, vol 42, pp. 30-37, (2003).

[31] S. Breer and K. Buse, "Wavelength demultiplexing with volume phase holograms in photorefractive lithium niobate". *Applied Physics. B*, vol. 66, pp. 339-345 (1998).

[32] S. Breer, H. Vogt, I. Nee, and K. Buse, "Low-crosstalk WDM by Bragg diffraction from thermally fixed reflection holograms in lithium niobate". *Electronics Letters*, vol. 34, pp. 2419-2421 (1999).

[33] G. Meltz, W. W. Morey, and W. H. Glenn, "Formation of Bragg gratings in optical fibers by a transverse holographic method". *Optics Letters*, vol 14, pp. 823- 825 (1989).

[34] N. Yoshimoto, S. Morino, M. Nakagawa, and K. Ichimura, "Holographic Bragg gratings in a photo responsive cross-linked polymer-liquid-crystal composite". *Optics Letters*, vol. 27, pp. 182-184 (2002).

[35] M. G. Moharam and T. K. Gaylord, "Diffraction analysis of dielectric surface relief gratings". *The Journal of the Optical Society of America*, vol. 72, pp. 1385-1392 (1982).

[36] M. G. Moharam, D. A. Pommet, E. B. Grann, and T. K. Gaylord, "Stable implementation of the rigorous coupled-wave analysis for surface-relief gratings: Enhanced transmittance matrix approach". *The Journal of the Optical Society of America*, A. vol. 12, pp. 1077-1086 (1995).

[37] S. M. Schultz, E. N. Glytsis, and T. Gaylord, "Design of a high-efficiency volume grating coupler for line focusing". *Applied Optics*, vol. 37, pp. 2278-2287 (1998).

[38] H. Tanaka, T. Kobayashi, T. Saitoh, Y. Suzuki and Shigeru Kawai, "Design Technique of Crossed Gratings for Beam Couplers in Large-Core Optical Fibers". *The Japanese Journal of Applied Physics*, vol. 41, pp. 4817–4820 (2002).

[39] M. Oh, S. Ura, T. Suhara, and H. Nishihara, "Integrated-optic focal-spot intensity modulator using electrooptic polymer waveguide". *The Journal of Lightwave Technology*, vol. 12, pp. 1569-1576 (1994).

[40] N. Eriksson, M. Hagberg, and A. Larsson, "Highly efficient grating-coupled surface emitters with single outcoupling elements," *IEEE Photonic Letters*, vol. 7, pp. 1394-1396 (1995).

[41] A. Alphones, "Double grating coupler on a grounded dielectric slab waveguide". *Optics Communications*, vol. 92, pp. 35-39 (1992).

[42] I. A. Avrutskii, A. S. Svakhin, V. A. Sychugov, and O. Parriaus, "High-efficiency single-order waveguide grating coupler". *Applied Optics*, vol. 15, pp. 1446-1448 (1990).

[43] J. C. Brazas, L. Li, and A. L Mckeon, "High-efficiency input coupling into optical waveguides using gratings with double-surface corrugation". *Applied Optics*, vol. 34, pp. 604-609 (1995).

[44] M. Hagberg, N. Eriksson, and A. Larsson, “High efficiency surface emitting lasers using blazed grating outcouplers”. *IEEE Journal of Quantum Electron*ics, vol. 32, pp. 1596-1605 (1996).

APPENDIX: PUBLICATIONS

Journals：

[1] D. Wu, W. Guo, Y. Yi, “Compound period grating coupler for double beams generation and steering”. *Applied Optics*.58 (2), 2019

[2] M. Ye, V. Ray, Y. Peng, W. Guo, Y. Yi, “Linear Polarization Distinguishing Metalens in Visible Wavelength”. *Optics Letters*. (Accepted on Dec.17, 2018)

Conference:

[1] D. Wu, W. Guo, Y. Yi, “Plasmonic Metal-Hybrid Hydrogen Sensor Based on Semiconductor Nanocrystal Micro Ring”. *MRS Advances*, 1-7. doi:10.1557/adv.2017.624

[2] Y. Yi, W. Guo, Y. Peng, “Enhancement of Light Trapping for Thin-Film Silicon Solar Cells”. *MRS Advances*, 2018 MRS Fall meeting & exhibit. (Accepted on Dec.3, 2018)